Quantum computing for neutrino-nucleus scattering

Alessandro Roggero,[1,*] Andy C. Y. Li,[2,†] Joseph Carlson,[3,‡] Rajan Gupta,[3,§] and Gabriel N. Perdue[2,‖]

[1]*Institute for Nuclear Theory, University of Washington, Seattle, Washington 98195, USA*
[2]*Fermi National Accelerator Laboratory, Batavia, Illinois 60510, USA*
[3]*Los Alamos National Laboratory, Theoretical Division T-2, Los Alamos, New Mexico 87545, USA*

(Received 16 January 2020; accepted 9 April 2020; published 27 April 2020)

Neutrino-nucleus cross section uncertainties are expected to be a dominant systematic in future accelerator neutrino experiments. The cross sections are determined by the linear response of the nucleus to the weak interactions of the neutrino, and are dominated by energy and distance scales of the order of the separation between nucleons in the nucleus. These response functions are potentially an important early physics application of quantum computers. Here we present an analysis of the resources required and their expected scaling for scattering cross section calculations. The current estimates of Trotter steps needed to achieve an energy resolution of 10 MeV and the number of CNOT gates for analyzing ^{40}Ar highlights the need for significant improvements in algorithms. We also examine simple small-scale neutrino-nucleus models on modern quantum hardware. In this paper, we use variational methods to obtain the ground state of a three nucleon system (the triton) and then implement the relevant time evolution. To tame the errors in present-day NISQ devices, we explore the use of different error-mitigation techniques to increase the fidelity of the calculations.

DOI: 10.1103/PhysRevD.101.074038

I. INTRODUCTION

Establishing the existence of "*CP* violation" in the lepton sector through neutrino oscillation experiments and testing the three-flavor neutrino framework at a long baseline experiment such as DUNE [1] are challenging tasks. Successful execution of these goals requires very fine controls on systematic uncertainties. Interaction model uncertainties will likely be the dominant systematic uncertainties in mature experiments, and further theory work is required to bring them under control [2,3].

Experiments use event generators, such as GENIE [4], NEUT [5], NuWro [6–8], and GiBUU [9], to connect final states observed in the detectors to the detailed underlying kinematics. There are two defining features for neutrino-nucleus interaction signals. First, the kinematic details of beam neutrinos are unknown on an event-by-event basis, and even the overall flux may be poorly constrained. Second, neutrino experiments favor heavy nuclear target materials to drive up event rates at the price of introducing very complex nuclear physics in the event reactions.

Because they are tools for understanding detector efficiency and backgrounds, event generators must simulate all types of constituents possible in the final state of an interaction and their momenta on an event-by-event basis. An ideal theory input would provide fully differential neutrino-nucleus cross sections with respect to the kinematics of every final-state particle, for all combinations of neutrino flavor and helicity, and for every nucleus in the target. Unfortunately, even the most sophisticated modern theory typically provides only the kinematics for the final-state lepton, and generally covers only a subset of the experimentally accessible phase space [10].

On classical computers, inclusive scattering in *ab initio* calculations are obtained via imaginary-time (Euclidean) correlation functions [11,12] or in factorization schemes [13]. These are typically relevant to inclusive scattering only, though some progress has been made toward exclusive processes [14]. Exact treatments, even for the ground state, scale exponentially in the nucleon number due to the Fermion sign problem. Constrained path algorithms are useful for low-lying states, but scattering has proven to be intractable on classical computers.

Since its first conceptualization [15], quantum computing has been seen to offer a potentially powerful tool for computing *ab initio* the time evolution of strongly correlated quantum systems, such as the ground state of nuclei, with controllable errors [16]. This is mostly due to the ease of incorporating fundamentally quantum effects such as entanglement and interference within its language, something that in general requires an exponential overhead on classical digital computers.

*roggero@uw.edu
†cli@fnal.gov
‡carlson@lanl.gov
§rajan@lanl.gov
‖perdue@fnal.gov

In an earlier publication [17], some of us proposed a quantum algorithm for digital quantum computers to efficiently estimate properties of (nuclear) final states in scattering events such as neutrino-nucleus reactions using a variant of quantum algorithms developed for quantum chemistry applications [18,19].

In this work, we start by carefully assessing in Sec. II the quantum resources needed for a minimally realistic description of a scattering process off a nucleus in the linear response regime. In particular, we first provide detailed implementations of quantum circuits simulating the time evolution needed for the algorithm presented in [17] in Sec. II A and also explore the use of an alternative approach in Sec. II B. While current quantum computing hardware is insufficient to do these calculations in full for relevant nuclei, especially without active error correction, our goal in Sec. III is to demonstrate proof of principle calculations that will motivate further research and development in this area.

II. LATTICE NUCLEAR MODEL

In this paper, we study systems using pionless effective field theory [20,21] on a lattice to explore quantum computing of nuclei and their response. We have chosen pionless effective field theory as it is the simplest possible model of nuclei and their interactions that exhibits some very basic properties of atomic nuclei. It consists of nonrelativistic nucleons interacting with a contact interaction that reproduces large scattering lengths at low energies.

At leading order it has nucleon-nucleon contact interactions describing the low-energy s-wave interactions in spin zero isospin one ($S=0$, $T=1$) and spin one isospin zero ($S=1$, $T=0$) nucleon pairs. The measured scattering length in $S=0$, $T=1$ (e.g., nn scattering) is approximately -18 fm, almost a bound state; while in the $S=1$, $T=0$ channel there is a weakly bound state, the deuteron, with a binding energy of 2.225 MeV. For initial studies, these simple pionless interactions are preferable since they can be efficiently implemented in a lattice basis; indeed, they have many similarities to a three-dimensional (3D) Hubbard model with attractive interactions, but with four species of fermions (neutrons and protons with spins up and down).

In addition to the two-nucleon interactions, a three-nucleon interaction is required to avoid collapse into deeply bound states [22,23]. Pionless effective field theory has been shown to approximately reproduce the binding of three and four nucleon systems, and to nearly produce weakly bound nuclei (with respect to break up into four-particle clusters) for $A=8$ and $A=16$ [24,25], as seen in nature. More complex interactions including virtual pions might be necessary for more accurate studies of lepton-nucleon interactions, as these provide fits to NN scattering data up to momenta of several inverse Fermi (see, e.g., [26–28]).

TABLE I. Hamiltonian parameters, corresponding to a lattice spacing $a=1.4$ fm, taken from [29].

t [MeV]	C_0 [MeV]	D_0 [MeV]
10.5794	−98.2265511	127.839693

The resulting lattice Hamiltonian for the pionless theory is

$$H = 2DtA - t\sum_{f=1}^{N_f}\sum_{\langle i,j\rangle}^{M}[c_{i,f}^{\dagger}c_{j,f} + c_{i,f}^{\dagger}c_{j,f}] + \frac{1}{2}C_0\sum_{f\neq f'}^{N_f}\sum_{i=1}^{M} n_{i,f}n_{i,f'} + \frac{D_0}{6}\sum_{f\neq f'\neq f''}^{N_f}\sum_{i=1}^{M} n_{i,f}n_{i,f'}n_{i,f''}, \quad (1)$$

where A is the number of nucleons, D the space dimension, N_f the number of fermionic species, and M the number of lattice sites. C_0 and D_0 describe the strengths of the attractive and repulsive two- and three-nucleon interactions, respectively. Here we assume the $S=0$, $T=1$ and $S=1$, $T=0$ scattering lengths are the same. If the box size is L and $M=N_L^D$, the kinetic energy parameter is $t=\hbar^2/2ma^2$ with the lattice spacing $a=L/N_L$. For the calculations presented in this section we use the numerical values reported in Table I (obtained from [29]) and corresponding to a lattice spacing of $a=1.4$ fm.

We can encode the Fock space with $\Omega = N_f \times M$ fermionic modes into Ω qubits using the Jordan-Wigner [30] transformation to obtain the mapping

$$n_q \equiv c_q^{\dagger}c_q = \frac{1-Z_q}{2} \quad (2)$$

and

$$c_q^{\dagger}c_p + c_p^{\dagger}c_q = -\frac{1}{2}X_qZ_{q+1}\cdots Z_{p-1}X_p - \frac{1}{2}Y_qZ_{q+1}\cdots Z_{p-1}Y_p. \quad (3)$$

In Eq. (3), we use X_q, Y_q, and Z_q to denote the corresponding Pauli matrix acting on qubit q, and the dots indicate Pauli Z matrices on the qubits along the chosen normal ordered path connecting the qubit for orbital q with the qubit for orbital p (for more details see, e.g., [18]). In this work we order the qubit placing next to each other the N_f qubits representing the same lattice site and different spin-isospin quantum numbers. This choice (equivalent to

the mapping used in early works on quantum chemistry such as [31]) is particularly convenient in our case due to the presence of the three-body interaction which requires one to couple triplets of fermions at the same lattice point. This is a different situation from the one encountered in quantum chemistry where a different mapping focusing on the kinetic energy is usually chosen (see, e.g., [32]).

The nuclear Hamiltonian can now be written entirely in terms of Pauli operators. Starting from the kinetic energy component

$$K = -t\sum_{f=0}^{N_f}\sum_{\langle i,j\rangle}^{M}[c_{i,f}^{\dagger}c_{j,f} + c_{i,f}^{\dagger}c_{j,f}] = -t\sum_{f=0}^{N_f}\sum_{i=0}^{M-1}\sum_{j\in NN(i)}[c_{i,f}^{\dagger}c_{j,f} + c_{i,f}^{\dagger}c_{j,f}] \tag{4}$$

we find explicitly

$$K = \frac{t}{2}\sum_{f=0}^{N_f-1}\sum_{i=0}^{M-1}\sum_{j\in NN(i)}(X_{N_f i+f}Z_{N_f i+f+1}\cdots Z_{N_f j+f-1}X_{N_f j+f} + Y_{N_f i+f}Z_{N_f i+f+1}\cdots Z_{N_f j+f-1}Y_{N_f j+f}), \tag{5}$$

where in the expressions above $NN(i)$ are the indices of the nearest neighbors of lattice site i. In turn, the potential can be written as the following diagonal operator:

$$\begin{aligned} V = {} & \frac{M}{4}\left(\frac{N_f(N_f-1)}{2}\right)\left(C_0 + \frac{N_f-2}{3}D_0\right) \\ & - \frac{N_f-1}{4}\left(C_0 + \frac{N_f-2}{2}D_0\right)\sum_{i=0}^{M-1}\sum_{f=0}^{N_f-1}Z_{4i+f} \\ & + \frac{C_0 + (N_f-2)D_0}{4}\sum_{i=0}^{M-1}\sum_{f=0}^{N_f-1}\sum_{f'>f}Z_{4i+f}Z_{4i+f'} \\ & - \frac{D_0}{4}\sum_{i=0}^{M-1}\sum_{f=0}^{N_f-1}\sum_{f''>f'>f}Z_{4i+f}Z_{4i+f'}Z_{4i+f''}, \end{aligned} \tag{6}$$

which, for the common case with $N_f = 4$, simplifies to

$$\begin{aligned} V = {} & M\left(\frac{3}{2}C_0 + D_0\right) - \frac{3}{4}(C_0 + D_0)\sum_{i=0}^{M-1}\sum_{f=0}^{3}Z_{4i+f} \\ & + \frac{C_0 + 2D_0}{4}\sum_{i=0}^{M-1}\sum_{f=0}^{3}\sum_{f'>f}Z_{4i+f}Z_{4i+f'} \\ & - \frac{D_0}{4}\sum_{i=0}^{M-1}\sum_{f=0}^{3}\sum_{f''>f'>f}Z_{4i+f}Z_{4i+f'}Z_{4i+f''}. \end{aligned} \tag{7}$$

Note that this operator is composed of a sum of

$$N_V = MN_f\left(1 + \frac{N_f-1}{2}\left(1 + \frac{N_f-2}{3}\right)\right) \tag{8}$$

mutually commuting operators while the kinetic energy term is composed of a possibly much larger number of mutually noncommuting operators. In this work we will consider two different breakups of the Hamiltonian: one where we separate all the $N_K = 4DMN_f$ terms in the expansion of the kinetic energy from a single potential energy term and one where we simply separate the kinetic and potential energy terms and treat each one exactly (cf. split-operator step in [33]). In the following we will refer to these splitting as α and β.

As we have anticipated in the Introduction, the main observables we are seeking are semiexclusive cross sections for a neutrino to scatter off a nucleus. A related but easier to compute quantity of interest is the response function

$$S(\omega) = \sum_f \delta(\omega - (E_f - E_0))\langle 0|O^{\dagger}|\Psi_f\rangle\langle\Psi_f|O|0\rangle, \tag{9}$$

which directly measures the inclusive cross section. The operator O in the above expression represents the electroweak excitation operator of the incoming neutrino, while $\{|\Psi_f\rangle\}$ and $\{E_f\}$ are the eigenstates and eigenvalues of a nuclear Hamiltonian like (1). In [17] we show how, by a slight modification of quantum algorithms developed for the estimation of $S(\omega)$ [18,19], one can set up a quantum computation to sample efficiently the most important final states of a neutrino-nucleus collision. The dominant cost in computing the cross section comes from the need to perform time evolution, and we dedicate the next subsection to characterize, for a realistic setup, how large this cost actually is. We finish this section by exploring an alternative approach based on the technique of qubitization [34], which provides an optimal asymptotic cost.

A. Time evolution

The cost of our original scheme [17] is dominated by the implementation of the time evolution unitary operator generated by this Hamiltonian controlled with an ancilla qubit. In the following we will estimate the computational cost of the algorithm by looking at the number of expensive operations (CNOTs and single qubit rotations[1]) needed to achieve some target accuracy in the inclusive response. We will account for the ancilla control of the time-evolution unitary by considering every rotation to be a controlled one which we implement in a standard way [see Eq. (A4) in Appendix A]. Note that we can easily extend parallelization even when rotations are controlled by ancillas as explained in [35].

In this section we will mostly consider product formulas: in particular, we will study in detail both linear and

[1]For definitions of quantum gates see eg. [62].

quadratic Trotter-Suzuki breakups and comment on the possible beneficial use of qubitization at the end of the section. We remind the reader that other techniques have been developed beside these, an important one being, for instance, the Linear Combination of Unitaries (LCU) method and its variants [36,37]. Since the implementation of the LCU method comes with a possibly much larger overhead in qubit count (see, e.g., [38] for a detailed study of a single Hamiltonian), we will not explore its use further in this first work.

1. Product formulas: Number of steps

Product formulas obtained from the Trotter-Suzuki decomposition [39,40] are essentially small-time approximations of the time-evolution unitary operator $U(t) = \exp(-itH)$ with additive error $\delta_{TS}(t) = \mathcal{O}(t^\gamma)$ for some $\gamma > 1$ (e.g., $\gamma = 2$ for the linear breakup). This implies that in order to perform a simulation lasting a total time τ with bounded error we will need to divide the total time interval $[0, \tau]$ into r segments and use in each one the approximate evolution operator to obtain

$$\begin{aligned}\delta_\tau &= \|e^{-i\tau H} - \tilde{U}(\tau/r)^r\| \\ &\leq r\|e^{-i(\tau/r)H} - \tilde{U}(\tau/r)\| = \mathcal{O}(r^{1-\gamma}),\end{aligned} \tag{10}$$

with $\tilde{U}(t)$ the approximate propagator. In general the norm appearing in Eq. (10) is the standard operator (or spectral) norm. For our application we are interested in systems with a fixed number of nucleons and both the Hamiltonian and every single term in either the α and β splitting commutes with the baryon number operator. We will consider then a *physical* norm defined as

$$\|O\|_{\text{phys}} = \sup\{\|O|\psi\rangle\|_2 : |\psi\rangle \text{A-baryon state}\}. \tag{11}$$

In other words, physical norms only take into account quantum states which respect the symmetry of the Hamiltonian and the initial conditions. Note that more generally we could restrict the class of physical states using additional symmetries (i.e., isospin) resulting in an even tighter norm since $\|O\|_{\text{phys}} \leq \|O\|$. This definition is very convenient in our case since it allows us to define a reasonable lower bound for the base time $\tau = 2\pi/\Delta H$ that we need in the Quantum Phase Estimation (QPE) part of the algorithm. In fact it is sufficient to provide a physical upper bound on the maximum spread in energy attainable in an A body system as

$$\begin{aligned}\Delta H &= E_{\max} - E_{\min} \\ &= \|K\|_{\text{phys}} + \|V_2\|_{\text{phys}} + \|V_3\|_{\text{phys}} + Ab_{\max},\end{aligned} \tag{12}$$

where $b_{\max}$ is the nuclear binding energy at saturation density and we have used the estimate $|E_{\min}| \leq Ab_{\max}$ for the lowest energy value. An even better bound can be obtained by considering $\|V\|_{\text{phys}} = \|V_2 + V_3\|_{\text{phys}}$ which is smaller due to the opposite signs in the interaction terms [see Eq. (B9) in Appendix B].

As a simple starting point we now consider the linear order Trotter-Suzuki product formulas of the form

$$U_L^\alpha(\tau) = \prod_k^{N_K} e^{-i\tau K_k} e^{-i\tau V}, \tag{13}$$

for the α splitting, where we used the expansion $K = \sum_k^{N_K} K_k$ for the kinetic energy operator, and

$$U_L^\beta(\tau) = e^{-i\tau K} e^{-i\tau V}, \tag{14}$$

for the β splitting. Higher order expressions with better error bounds can also be obtained [see Eq. (B20) and discussion in Appendix B]. Here we recall only the second order expansions that are mostly employed in this work: for the α splitting these are

$$S_\alpha(\tau) = e^{-i\frac{\tau}{2}V} \prod_{k=1}^{N_K} e^{-i\frac{\tau}{2}K_k} \prod_{k=N_K}^{1} e^{-i\frac{\tau}{2}K_k} e^{-i\frac{\tau}{2}V}, \tag{15}$$

while for the β splitting we consider the two options

$$S_\beta^{K+V}(\tau) = e^{-i\frac{\tau}{2}K} e^{-i\tau V} e^{-i\frac{\tau}{2}K} \tag{16}$$

and

$$S_\beta^{V+K}(\tau) = e^{-i\frac{\tau}{2}V} e^{-i\tau K} e^{-i\frac{\tau}{2}V}, \tag{17}$$

whose implementation requires almost the same number of quantum gates whenever the number of intervals is large (cf. discussion in [33]).

In general the error on these types of product formulas depends on the commutator between the different terms in the sum defining the Hamiltonian [39]. One can, however, obtain a rigorous (but not very tight) upper bound on the total error in Eq. (10) using only the norms of those operators (see, e.g., [38,41]).

Using the analytical bounds given in Eqs. (B19) and (B22) for the linear and symmetric higher order formulas we have estimated the number of segments (Trotter steps) needed to achieve an energy error $\epsilon_\tau = \delta_\tau/\tau$ equal to half the frequency resolution $\Delta\omega$ for two different values of the total time interval τ: the base time $\tau_{\text{base}} = 2\pi/\Delta H$ (black and green lines) and the whole sequence of W evolutions for a total time of $\tau_{\text{tot}} = (2^W - 1) * \tau_{\text{base}}$ (red and blue lines) where the number of ancilla qubits W is obtained for a fixed resolution $\Delta\omega$ as

$$W = \left\lceil \frac{\Delta H}{\Delta\omega} \right\rceil. \tag{18}$$

We present in Fig. 1 the results obtained for both splitting methods at the target accuracy $\Delta\omega = 10$ MeV (for lower

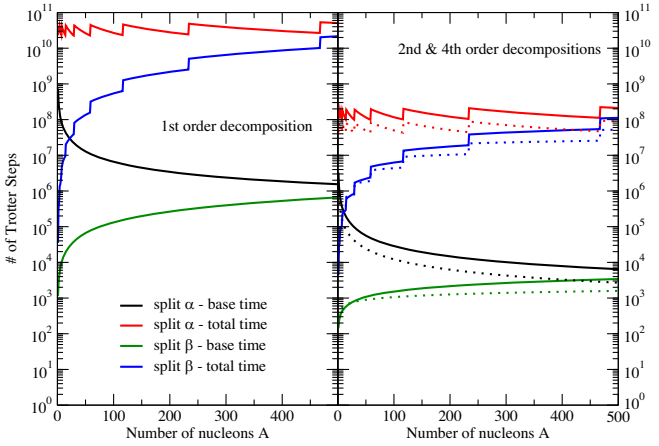

FIG. 1. Estimated number of Trotter steps for both splittings of the Hamiltonian and target resolutions $\delta\omega = 10$ MeV for Trotter-Suzuki formulas of different orders. The left panel shows the linear formulas Eqs. (13) and (14), and the right panel shows results for both a second order formula (solid lines) and a fourth order one (dotted lines).

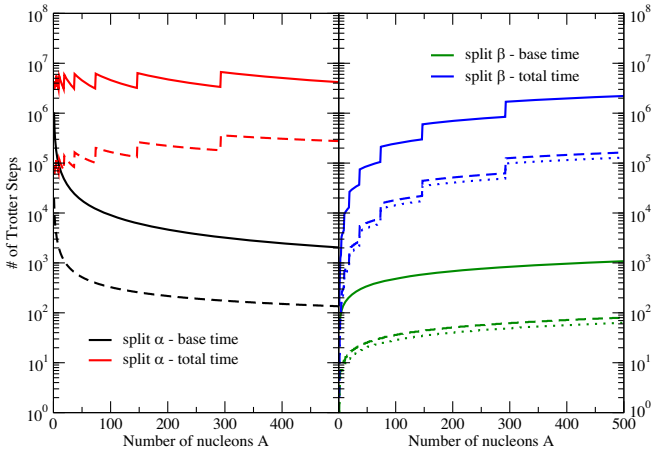

FIG. 2. Comparison of the analytical (solid lines) vs commutator bounds (dashed lines) $r_{2:A}$ and $r_{2:C}$ for the quadratic Trotter-Suzuki breakup with both splitting schemes (α for the left panel and β for the right one) at fixed target resolution $\Delta\omega = 100$ MeV. The dashed lines for the β splitting correspond to the choice $(V + K)$ while the dotted lines are for the complementary choice $(K + V)$ (see text for details).

accuracy the difference between second and fourth order formulas is much reduced).

We see that the fourth order formulas (represented as dotted lines in Fig. 1) provide an advantage only for big enough problems: for the better performing β splitting, for instance, the fourth order formula becomes advantageous after $A = 24$, whereas for lower target accuracy $\delta\omega = 100$ MeV (not shown) the breakeven point is shifted to $A = 234$.

Apart from their dependence on the norms of the Hamiltonian terms instead of their commutators, an important deficiency of the bounds used above is also their inability to differentiate between different ordering of operators in higher order formulas. We provide a more detailed discussion on the derivation of commutator bounds in Appendix B. Here, in Fig. 2, we show only the effect on the more efficient second product formulas Eqs. (15), (16), and (17). For all curves the target accuracy was fixed to $\Delta\omega = 100$ MeV for the two splitting methods.

We turn now into a more detailed discussion on the computational cost for a single time step needed to implement the time propagator using different implementation strategies. For both splitting methods we will need to design three different unitary operators (more details in Appendix B 3)

$$U_1(\tau) = e^{-i\tau V}, \quad U_2(\tau) = e^{-i\tau K}, \quad U_3(\tau) = \prod_{k=1}^{N_K} e^{-i\tau K_k}.$$

In our derivation we will consider the connectivity of qubits to follow a 2D square lattice topology and, even under this constraint, the implementation of the diagonal unitary U_1 is relatively simple (see Appendix B 3 a).

Because of its (mild) nonlocality, the most expensive term to implement is the hopping term. Depending on the splitting scheme, we will adopt (similar to the approach described in [33]) the fast fermionic Fourier transform (FFFT) algorithm [42] (or its variants [19,43]) for the implementation of splitting β. For the splitting α, we will employ a fermionic-SWAP network [43] to implement the product of the unitaries needed.

Results of the cost estimates for a realistic system with $M = 10^3$ and $N_f = 4$ are presented in Fig. 3. Note that

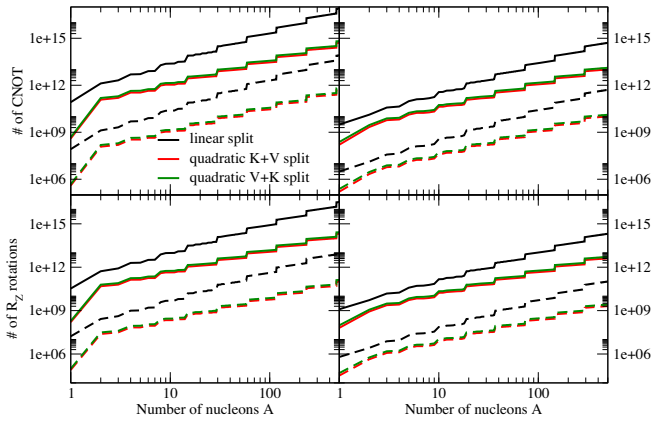

FIG. 3. Estimated gate count, in the CNOT + R_z basis, of the phase estimation kernel of the linear response algorithm of [17] as a function of the nucleon number. Shown are results for the β splitting and both first and second order Trotter decompositions. The left panel is for an energy resolution $\Delta\omega = 10$ MeV and the right is for $\Delta\omega = 100$ MeV. The solid lines correspond to the serial execution while parallelism is exploited for the dashed ones.

using the lattice spacing $a = 1.4$ fm (see Table I) this corresponds to a box with physical dimension $L = 14$ fm, more than enough to contain both a medium-mass target bound state and possible reaction final states. In this setup, performing the calculation for ^{40}Ar would require 4012 qubits (± 4 depending on target resolution and the particular implementation) and $\sim 10^{10}$ CNOT and $\sim 10^{9}$ rotation for the higher resolution $\Delta\omega = 10$ MeV and $\sim 5 \times 10^{8}$ CNOT and $\sim 10^{8}$ rotations at lower resolution $\Delta\omega = 100$ MeV. These estimates put a full computation of neutrino scattering off Ar at the same complexity level as factorizing a 1024-bit integer (cf. [38,44]) and possibly out of reach of near term NISQ devices. In the next section we explore possible improvements to this estimate using qubitization.

B. Different scheme using qubitization

At a modest (logarithmic) cost in the number of additional ancilla qubits, one can more efficiently calculate the eigenvalues and hence responses relevant to neutrino-nucleus scattering using a quantum algorithm generically termed qubitization [34]. Unlike the approach we proposed in [17] and described in the previous section, this algorithm avoids the implementation of the time evolution operator and any associated errors associated with the time step. Instead it employs a quantum walk operator known as a qubiterate [34].

One possible definition of this unitary, acting on both the system register and an additional register of ancilla qubits, is

$$Q = e^{i \arcsin(H/\lambda) R_Y}, \tag{19}$$

where $\lambda \geq \|H\|_1$ is a scaling factor needed to ensure the argument of the arcsin has norm bounded by one and, for every eigenvector of H, the operation R_Y acts nontrivially only on a two-dimensional subspace of the ancilla register's Hilbert space (see Appendix C for a more detailed exposition). This unitary operator can be implemented exactly using qubitization (see [34] and the discussion in Appendix C), which exploits the following decomposition (apart from a global phase) in terms of two basic unitaries V_P and V_S and a reflection

$$Q = V_P^\dagger \Pi_0 V_P V_S, \tag{20}$$

where $\Pi_0 = (|0\rangle\langle 0| - \mathbb{1})$ is a reflection around $|0\rangle$, the operation V_P is called the *prepare* and V_S the *select* unitary [see Eqs. (C3) and (C4) in Appendix C].

Schemes for time evolution based on this idea provide optimal scaling for the computational complexity [45], here instead we follow a different procedure. Since the spectra of $U(t)$ and the qubiterate of Eq. (19) are similar, the idea (originally proposed in [46,47]) is now to use the exact qubiterate for doing phase estimation instead of the (approximate) time evolution operator. The first main difference is that, due to the rescaling, the number of ancilla qubits used for phase estimation (or equivalently the number of applications of the qubiterate) will need to increase accordingly. In particular, we have, for target precision $\Delta\omega$, the result

$$W_q = \left\lceil \log_2\left(\frac{\lambda}{\Delta\omega}\right) \right\rceil \sim \log_2\left(\frac{\lambda}{\Delta H}\right) W, \tag{21}$$

where W was the previous result for the qubit count using time evolution. The second main difference is that in order to obtain the final state of the scattering process we need to perform a rotation from the eigenvectors of the qubiterate to those of H, and one way to do this is to use the strategy proposed in [46].

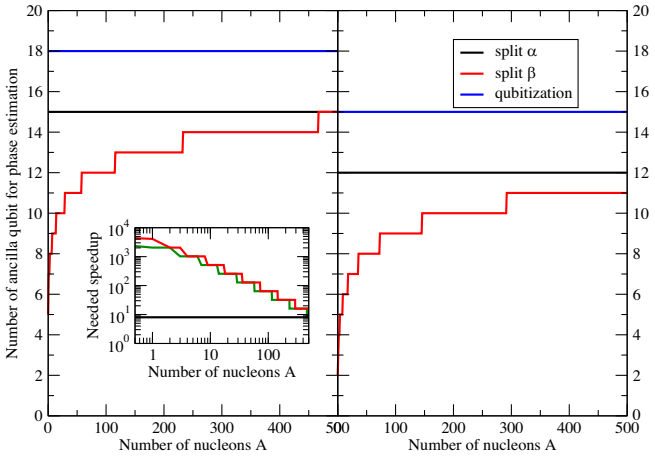

FIG. 4. Estimated number of ancilla qubit needed for a fixed target precision of $\Delta\omega = 10$ MeV (left panel) and 100 MeV (right panel) using either time evolution with both split methods described in the main text and qubitization. The inset shows the needed speedup the qubiterate needs to show with respect to the time evolution circuit for the base time $\tau = 2\pi/\Delta H$ in order to be competitive.

In Fig. 4 we show the expected increase as a function of the number of nucleons for two different target accuracies: $\Delta\omega = 10$ MeV in the left panel and $\Delta\omega = 100$ MeV for the right one. In the inset we show the ratio between the number of applications of the qubiterate vs the number of applications of the base time evolution $U(\tau)$ for time $\tau = 2\pi/\Delta H$; it represents the needed speedup in gate count of the qubiterate with respect to $U(\tau)$ for the qubitization strategy to be worth it. As expected the difference between the α-split method and qubitization does not depend on the particle number, and the ratio is stable at 8 [meaning the implementation of Eq. (19) can require up to 8 times more gates than time evolution as shown by the black line in the inset]. For the β-split scheme, this ratio is 128 in the ^{40}Ar region.

To employ the qubiterate Q for the QPE part of the algorithm we need to implement the operation ${}_cQ$

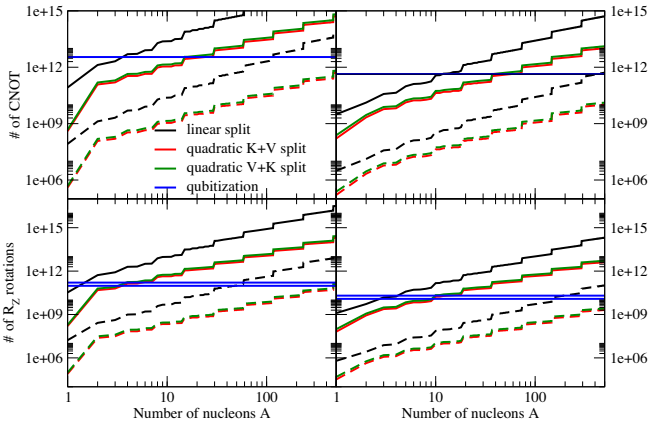

FIG. 5. Estimated total gate count in CNOT + R_Z basis for the β splitting and the variant based on the qubiterate.

controlled on an ancilla. Using the decomposition presented above in Eq. (20), we can write

$$ {}_cQ = {}_cV_{Pc}^{\dagger}\Pi_{0c}V_{Pc}V_S = V_{Pc}^{\dagger}\Pi_0 V_{Pc}V_S, \tag{22}$$

where, in the second equality, we removed the controls on the *prepare* (this simplification was proposed before; see, for instance, Ref. [38]). One can simplify this further and drop the control on the *select* unitary if we choose to define $V_S|0\rangle = |0\rangle$ when acting on the $|0\rangle$ state of the ancilla register and perform an initial controlled-*prepare* when initializing the ancilla system.

Using the implementation proposed in [38] (and presented in more detail in Appendix C 1 for completeness) we found the resource estimates reported in Fig. 5. In these results we considered only the cost for implementing the *prepare* unitary V_P together with the control circuit of the *select* unitary V_S and are therefore lower bounds on the resource cost. We find that, even though this methodology has optimal asymptotic scaling [34], the inherent costs of implementing qubitization is already expensive enough to lose the competition with the parallel circuits devised above.

A possible way to reduce the gate count needed to successfully calculate the response of ^{40}Ar would be to exploit stochastic algorithms such as the recently proposed qDRIFT [48]. We plan to explore this possibility in future work.

III. TRITON TOY MODEL

For a simplified problem on present-day computers, we consider a system of 3 nucleons on a 2×2 lattice with periodic boundary conditions. One of the nucleons is chosen to be static (infinite mass) on a specific lattice site. This can be thought of as a triton (a nucleus with one proton and two neutrons), or the static nucleon can be thought of as providing a static field in which the interacting pair propagates.

Calculations of the realistic response demonstrate that two-nucleon physics incorporates much of the information about nuclear response [14], making even such a simple problem important. The fixed particle is ultimately a source of additional final-state scattering which in traditional event generators is included as a semiclassical evolution. Quantum computers will eventually be able to treat the full problem for A nucleons quantum mechanically. In the near term, these kinds of models allow for tests of the generator paradigm, where at the vertex a struck nucleon or nucleon pair is treated quantum mechanically and then propagates through the rest of the nucleus in a semiclassical manner.

The Hamiltonian we use is

$$\begin{aligned} H = &-t\sum_{f=1}^{N_f}\sum_{\langle i,j\rangle} c_{i,f}^{\dagger}c_{j,f} + 2dtA \\ &+ U\sum_{i=1}\sum_{f<f'}^{N_f} n_{i,f}n_{i,f'} + V\sum_{f<f'<f''}^{N_f}\sum_{i=1} n_{i,f}n_{i,f'}n_{i,f''} \\ &+ U\sum_{f=1}^{N_f} n_{1,f} + V\sum_{f<f'}^{N_f} n_{1,f}n_{1,f'}, \end{aligned} \tag{23}$$

where the static nucleon is placed on lattice site 1.

For this example we use only two dynamical particles, and we set $N_f = 2$. On a 2×2 lattice with $N_f = 2$ modes we find that the Hamiltonian in second quantization with the simple Jordan-Wigner mapping described above (one qubit for each single-particle orbital) will require a total of eight qubits to encode the problem. We are, however, interested in the sector containing $A = 2$ dynamical particles whose dimension is only 16 and should require just four qubits. In the following we will use a first-quantized mapping that accomplishes this minimal encoding. We note in passing that, even though this simple problem could be solved with ease using modest classical computational resources, attempting to solve it on current quantum devices is still of fundamental importance in order to assess the capabilities of today's quantum computers and at the same time devise solutions for possible issues we will face.

We can use two qubits per particle to store its lattice location in the following way (see also Fig. 6):

$$|1\rangle \equiv |\downarrow\downarrow\rangle \quad |2\rangle \equiv |\downarrow\uparrow\rangle \quad |3\rangle \equiv |\uparrow\downarrow\rangle \quad |4\rangle \equiv |\uparrow\uparrow\rangle. \tag{24}$$

The hopping term in the kinetic energy is very simple and takes the form

$$H_{\text{hop}} = H_{\text{hop}}^{A} \otimes \mathbf{1}_B + \mathbf{1}_A \otimes H_{\text{hop}}^{B}, \tag{25}$$

where

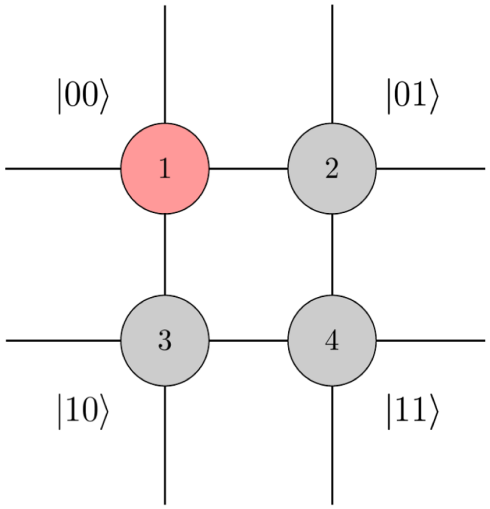

FIG. 6. Qubit mapping for a single fermion.

$$H^A_{\text{hop}} = -2t \begin{pmatrix} 0 & 1 & 1 & 0 \\ 1 & 0 & 0 & 1 \\ 1 & 0 & 0 & 1 \\ 0 & 1 & 1 & 0 \end{pmatrix} \equiv -2t(X_1 \otimes \mathbf{1}_2 + \mathbf{1}_1 \otimes X_2), \tag{26}$$

where X_k is the Pauli-X operator applied to qubit k and the additional factor of 2 comes from the periodic boundary conditions. The total hopping term reads then

$$H_{\text{hop}} = -2t(X_1 + X_2 + X_3 + X_4), \tag{27}$$

where we dropped the identity operators for simplicity.

For the diagonal part, we can extract an overall piece proportional to the identity on all qubits with coefficient $8t + U$; to change the diagonal element corresponding to the state $|11\rangle$ we add $2U + V$; and when both particles are on different lattice sites and neither of which is 1 by adding $-U$.

The procedure to do this in terms of Pauli operators is very simple as shown by a couple of examples. Consider the two sets of operators

$$M_k = \frac{\mathbb{1}_k - Z_k}{2}, \qquad \Pi_k = \frac{\mathbb{1}_k + Z_k}{2}. \tag{28}$$

In terms of these operators we have

$$\begin{aligned}(2U + V)|11\rangle\langle 11| &= (2U + V)|\downarrow\downarrow\downarrow\downarrow\rangle\langle\downarrow\downarrow\downarrow\downarrow| \\ &= (2U + V)[\Pi_1 \otimes \Pi_2 \otimes \Pi_3 \otimes \Pi_4]\end{aligned} \tag{29}$$

and

$$\begin{aligned}-U|23\rangle\langle 23| &= -U|\downarrow\uparrow\uparrow\downarrow\rangle\langle\downarrow\uparrow\uparrow\downarrow| \\ &= -U[\Pi_1 \otimes M_2 \otimes M_3 \otimes \Pi_4]\end{aligned} \tag{30}$$

and so on for the other terms.

The limiting case, $V = -4U$, results in the following simplified Hamiltonian:

$$\begin{aligned}H = 8t + \frac{U}{2} - 2t\sum_{k=1}^{4} X_k \\ - \frac{U}{4}(Z_1Z_4 + Z_2Z_3) - \frac{U}{4}\sum_{i<j<k} Z_iZ_jZ_k.\end{aligned} \tag{31}$$

This choice of parameters is motivated by the requirement that the three-body repulsive term be larger than the three pair interaction energy in order to prevent the collapse of the bound state. In the following we will consider the following numerical values: $t = 1.0$, $U = -7.0$, and $V = 28$.

A. State preparation

In this work we use the Variational Quantum Eigensolver (VQE) algorithm [49] to prepare an approximate ground state using a minimal number of quantum operation. We will define a parametrized trial state $|\Psi(\vec{\alpha})\rangle$, with real parameters $\vec{\alpha}$ by applying a parametrized unitary $U(\vec{\alpha})$ to the reference state $|0\rangle$. The optimal value of these parameters is obtained by solving the variational problem

$$\min_{\vec{\alpha}} E(\alpha) \quad \text{with} \quad E(\alpha) = \langle\Psi(\vec{\alpha})|H|(\vec{\alpha})\rangle, \tag{32}$$

which is guaranteed to provide an upper bound $E(\vec{\alpha}_{\text{opt}})$ to the true ground state energy E_0.

A simple trial state that is also economic to optimize can be obtained by considering the following circuit:

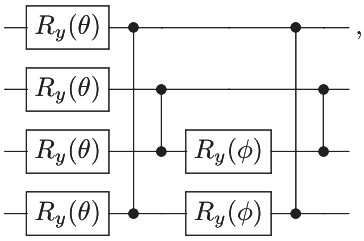

(33)

parametrized by two angles (θ, ϕ) and requires only linear connectivity to be implemented.

The entanglement structure is inspired by the Unitary Coupled Cluster wave function that we would construct in the absence of the three-body terms in the Hamiltonian of Eq. (31) and by the fact that the Hamiltonian is real in the computational basis.

As can be seen from Table II, despite its simplicity this trial state has only about 10% error in the energy and sum

TABLE II. Results for the ground state energy and the static structure factor. Errors in the experimental result account for statistical fluctuations only. Here QPU stands for Quantum Processing Unit.

	Energy	S(0,1)	S(1,0)	S(1,1)
Exact g.s.	−4.843	2.038	2.038	2.054
Trial state	−4.415	2.024	2.024	2.366
QPU bare	−2.645(15)	2.0290(23)	2.0242(24)	2.1572(25)
QPU corr	−4.4187(98)	1.9993(35)	1.9926(36)	2.2789(51)
QPU sym	−4.322(33)	2.0105(69)	2.0030(45)	2.3341(95)

rules are comparable with the exact ground state. In the results presented in this work, the optimization of the two parameters of our trial state is performed off-line using a simulator locally. After extensive experimentation we, in fact, determined that this was the most efficient and accurate strategy: this is possibly a consequence of the simplicity of the problem. In the third and fourth rows of Table II, we present the results obtained by estimating the properties of the state generated on a real quantum processor. In particular, we mapped our four computational qubits into qubit 5, 0, 1, and 6, respectively, on the IBMQ 20 qubit machine Poughkeepsie [50]. In the first line denoted "QPU bare," we report the bare result obtained from a statistical analysis of 324 runs (each run is a full experimental execution of the quantum algorithm on the device), each comprising 8192 repetitions (shots), but without performing any form of error mitigation. The next line shows the much better result obtained by mitigating both readout noise and the decoherence effect coming from the CNOT gates (see Sec. III C for more details).

In the last line of Table II we report instead the (error mitigated) results obtained from 108 runs using a more symmetric version of the above trial state shown below

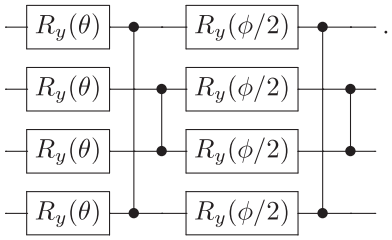

(34)

The added symmetry seems to bring some advantage in the (1, 1) sum rule but the added noise caused by additional noisy rotations seems to be detrimental for the energy.

B. Real time dynamics

In the general case ($V \neq 0$ and $V \neq -4U$) one can use the result from [32] which implies that we would need 14 CNOT and 15 single qubit rotations for the diagonal part of the propagator plus 4 more X rotations for the hopping term resulting in 14 CNOT and 19 rotations. [With more constraints such as having a circle topology this can increase to 16 CNOT. See also Eq. (B47).] For the special case $V = -4U$ a simpler expression can be found

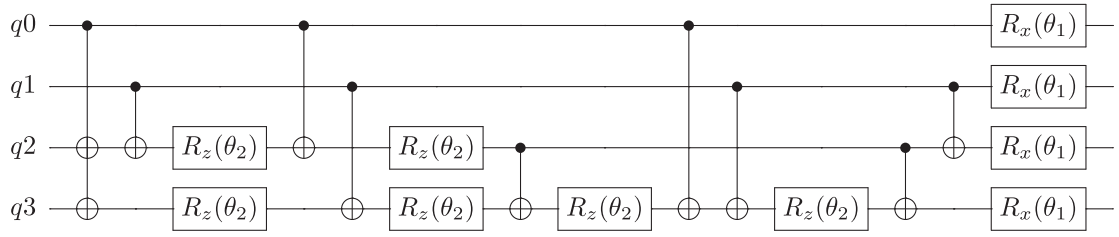

(35)

with $\theta_1 = 4t\tau$ and $\theta_2 = \tau U/2$. This implementation requires 10 rotations and 10 CNOT. The problem with this expression is that it requires entangling gates on all but one pair of qubits (i.e., in the expression above there is no connection $q_0 \leftrightarrow q_1$ but all others).

With the additional connectivity constraints of the IBM QPU "Poughkeepsie" we found the following circuit

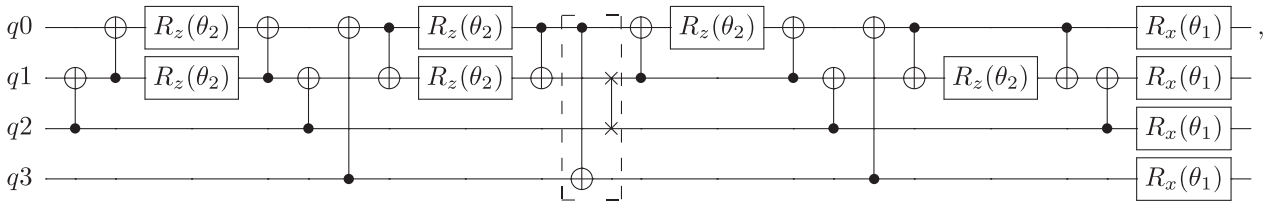

(36)

where in the box denoted with the dashed line we perform a swap of both $q1 \leftrightarrow q2$ and $q0 \leftrightarrow q3$. Of the latter two of the three CNOT involved in the operation cancel with neighboring gates.

We can now show results for some dynamical property. In Fig. 7 we plot the three-body contact density

$$C_3(t) = \langle \Psi(t)|\Pi_{0000}|\Psi(t)\rangle \equiv |\langle 0000|\Psi(t)\rangle|^2 \quad (37)$$

as a function of time starting at time $t = 0$ with the trial state of the previous section. The expression above measures the probability of the three nucleons to be on the same site (the state $|0000\rangle$ in our basis). The time evolution is obtained by means of the linear Trotter decomposition described above and therefore starts to deviate considerably from the exact time evolution at around $t \sim 0.04$.

In the left panel we show, together with the exact result with the solid blue line, the bare results obtained by running the algorithm either on the actual quantum device (black circles) or on a local virtual machine (VM) employing a noise model designed to mimic the behavior of the real device (red squares) [51]. The hardware results were obtained using the Poughkeepsie QPU (backend version 1.2.0) over a three weeks period starting on August 23, 2019 and adopting the mapping $(q_0, q_1, q_2, q_3) \to (q_5, q_0, q_1, q_6)$ from the four logical qubits to the hardware ones. The corresponding results on the Virtual Machine used the noise model configured with the calibration data on September 11, 2019.

In both cases, we see that the results tend to relax toward the classical completely depolarized value of $1/16$ (dashed brown line) but that we can still detect a reasonable signal. The observed large bias at small times might be attributable to control errors in the device and unfortunately does not allow this particular set of qubits to be used to perform multiple Trotter steps as the error in the useful region is too large. Different choices for the logical to physical qubit mapping can improve the fidelity in the small-time region.

We now turn our attention to the right plot in Fig. 7. As explained in more detail in the next subsection, we have attempted to mitigate the systematic errors caused by hardware noise by performing three independent noise extrapolations and comparing them to assess both the stability of our extrapolations and the stability of the machine during a particular run. Whenever the different schemes do not agree, we increase an error counter and filter the final results using the total error count as a metric for the run quality. In the right panel of Fig. 7 we present the result after this mitigation procedure for different values of the error count starting from 0 (filter $A0$ in the figure) up to 2 errors (filter $A2$). In addition to the results obtained on hardware with this approach, we also plot the results at the 2 error level of accuracy for both the synthetic data produced by the VM (the red squares on the left panel) and the results obtained by relaxing the consistency checks at the 2σ level of precision. We see that the simpler noise model implemented in the VM can be completely mitigated using this strategy while for the real hardware case there seems to be a problem in the time region $t \in [0.3\text{–}0.4]$ where no results with good enough quality can be obtained. We will provide a possible explanation for this phenomenon after discussing in more details the mitigation procedure adopted in our work.

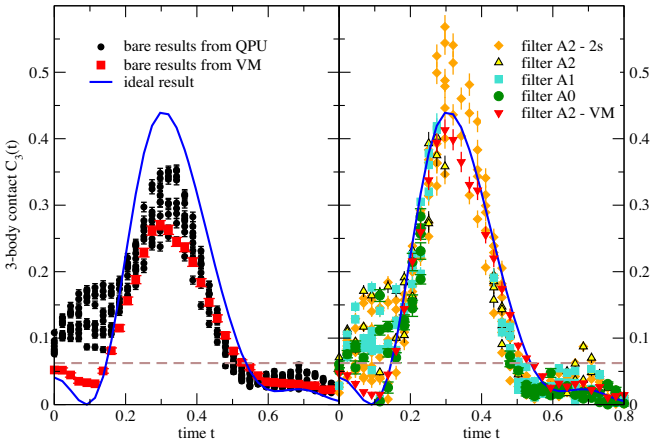

FIG. 7. Probability of finding the three nucleons on the same site as a function of time using both a real QPU (black circles) and a simulated VM (red squares). See text for a description of the left panel.

C. Error mitigation

In our final results such as those shown in Fig. 7 we perform two types of error mitigation: a readout correction on the measured distributions and a noise extrapolation assuming that the dominant noise channel is the one associated with the execution of a CNOT gate (cf. [52–54]). In the future we would also like to investigate the use of twirling (see, e.g., [55]) to contrast the control errors affecting the small-time results shown above.

The correction for measurement errors is obtained by first attempting a simple procedure where we assume errors are qubit-independent and described by a distortion of the two measurement operators

$$\begin{aligned} |\tilde{0}\rangle\langle\tilde{0}| &= (1-p_0)|0\rangle\langle 0| + p_1|1\rangle\langle 1|, \\ |\tilde{1}\rangle\langle\tilde{1}| &= p_0|0\rangle\langle 0| + (1-p_1)|1\rangle\langle 1|, \end{aligned} \quad (38)$$

and use the results of two calibration measures where we prepare both basis states and perform a Z measurement to obtain the empirical error matrix

$$N_k = \begin{pmatrix} 1-p_0 & p_1 \\ p_0 & 1-p_1 \end{pmatrix}. \quad (39)$$

Here, the subscript k identifies a particular qubit on the hardware. Noise-free results are then obtained by applying the inverse of this matrix to the measured distribution while the errors are propagated correctly in the process (see also [56] for more details on the procedure).

If this simple scheme produces an unphysical distribution (with, for example, negative entries), the central value of the corrected distribution is obtained using a least squares inversion and a generalized procedure where the calibration is obtained from a set of 2^n state preparation as implemented in qiskit Ignis [51], while the error is estimated from the simpler procedure used before. In our experience, violations of the independent qubit error model are rather rare. To track the quality of an experimental run we will add one error if the simple procedure fails (now the threshold is set to 2σ for the check).

To obtain an estimate of the noise-free result, we use the idea of noise amplification and extrapolation used successfully in the past [53,54,57]. The idea is simple: imagine a model for the parametric dependence of an observable M to the noise strength ϵ (for instance, a low order polynomial for small ϵ), we can control the noise strength accurately enough to produce estimates $M(k \times \epsilon)$ at a larger error rate (i.e., $k > 1$), and then we could extrapolate the result to the zero error limit.

In this work we employ three different strategies together:

(i) Richardson: in the regime where the circuit depth is very small and only a small number of errors are contaminating the results, it makes sense to look for a Richardson type extrapolation obtained by computing the exact polynomial interpolant of the noisy points we have (cf. [58]). At order 3, as in our case, we will obtain a cubic. The lowest order compatible with the higher ones (at the 1σ level) is considered the preferential one. If a result satisfying this compatibility is found, we increase the error count by one, drop the highest order point, and try again. If still no valid point is found, the Richardson extrapolation is deemed failed.

(ii) Polynomial: in the same small error regime if the rate is small enough, we should be able to fit multiple points with the same low order polynomial (cf. [53]). Here we attempt to perform polynomial fits up to third order of all the points (four in our case) available. As for the previous method we look for the lowest order fit with $\chi^2 \leq 1$ and compatible with the higher order fits. Similarly, failure over the four points increases the error count, and we try without the highest order point. If the procedure fails the second time, the polynomial fit is deemed failed.

(iii) Exponential: when the error rate is sufficiently large (or the gate count is), one could expect the results to decay exponentially towards the fully depolarized state (cf. discussion in [54,59]). We attempt a two point exponential fit to the results and, as for the methods above, look for compatibility at higher orders and raise the error count when this cannot be found.

A run is considered to have been executed successfully when at least one technique produces a good result. When comparing different successful extrapolations, priority is given to a good global linear fit. If none are available, we pick the set with the lowest error count and take an average of both mean and error.

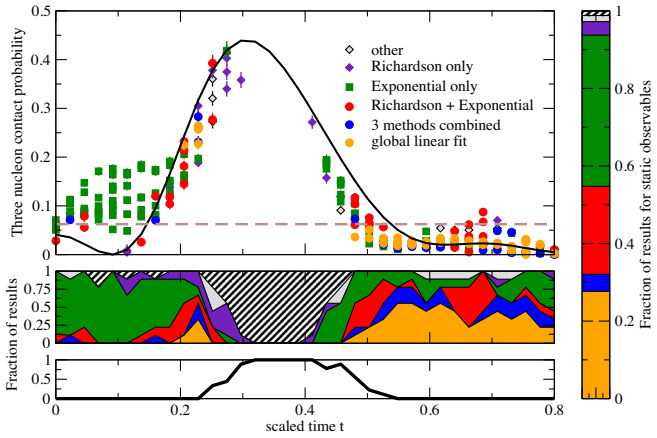

FIG. 8. Extrapolation procedures used to mitigate errors in the results for the three nucleon contact density $C_3(t)$ shown in Fig. 7. See main text for a description of the different panels.

Figure 8 shows the interplay between different extrapolation procedures. The main plot shows the error-mitigated probability of finding three nucleons on the same site with colors indicating the mitigation strategy employed. The central panel shows the ratios of runs mitigated with a particular strategy as a function of time. The legend of the main plot also applies here with the addition of the shaded area indicating failed runs where no stable extrapolation was possible. The bottom panel shows an estimate of the fraction of runs that have decohered (see details at the end of this section). Finally the right column shows the results for a set of nine static observables evaluated on the trial state showing the effect of reducing the circuit depth: for small circuits where the number of errors is not large, the small error expansion that motivates both the Richardson and polynomial extrapolations should hold in practice. Indeed, the results for static observables show that the exponential fit is preferred on less than about 40% of the calculations. When computing dynamical properties instead, the much longer circuit depth starts to favor the exponential extrapolation strategy apart from the results at late times where the magnitude of the observable is so close to the fully depolarized result that a global linear fit usually works.

In addition to the three-body contact, Eq. (37), obtained as the expectation value of the projector $P_{3B} = |0000\rangle\langle 0000|$ shown in Fig. 8, we have also computed the various two-body contacts. In particular, we use the projector

$$P_{2B\text{-dyn}} = |0101\rangle\langle 0101| + |1010\rangle\langle 1010| + |1111\rangle\langle 1111| \tag{40}$$

to estimate the probability $C_2^D(t)$ that the two dynamical particles can be found in the same lattice site apart from the special one, and the projector

$$P_{2B\text{-}sA} = |0001\rangle\langle 0001| + |0010\rangle\langle 0010| + |0011\rangle\langle 0011| \tag{41}$$

to compute the probability $C_2^A(t)$ that the first particle (tagged A here) is on the special lattice site while the other one is not (note that due to symmetry we will have the same result if we choose to tag particle B).

In addition to these three extrapolations, we also check for possible complete decoherence by first checking that the distribution obtained with the smallest number of CNOT has an overlap with the fully depolarized state of less than 0.9. We raise an error count if in the higher order results we find two distributions with overlap > 0.9. In this work we used the trace distance as an estimator of overlap

$$ovd = 1 - \frac{1}{2}\sum_{i=1,16}\left|\frac{1}{16} - p(i)\right|, \tag{42}$$

where $p(i)$ are the empirical (and readout error mitigated) probabilities. In general, it might be better to include the error information in the estimator, and we plan to explore different approaches in future work. For the set of runs using the mapping $[5, 0, 1, 6]$ we found that results were possibly decohered for time in the interval $t \in [0.25, 0.5]$, and this is the reason we were not able to determine robust estimators for $C_3(t)$ in that interval. This problem is not directly apparent while looking at the two-body contact densities since the error-free result is itself close to the decohered result and therefore the test above does not trigger within the chosen bounds. We can, however, clearly see that the extrapolated results obtained in the problematic region are indeed compatible with the dashed brown line corresponding to the value $1/16$ as expected.

To understand the systematic deviations of the experimental results from those expected in theory, we will now try to quantity the amount of entanglement generated in the time evolution. We will use different entanglement measures to study the correlations present in the four-qubit state. The first one is the entanglement entropy, which for a bipartite system described by the density matrix ρ_{AB} is defined as

$$S_A = -\mathrm{Tr}[\rho_B \ln(\rho_B)] = -\mathrm{Tr}[\rho_A \ln(\rho_A)] = S_B, \tag{43}$$

where $\rho_{AB} = Tr_{BA}[\rho]$ are reduced density matrices. The entropy will be zero when the state is separable along the partition (A, B). In the top panel of Fig. 11 we show the entanglement entropy for the local one-qubit density (S_k with $k = \{0, 1, 2, 3\}$) as a dashed black line and the two-qubit entropies S_{01} (red line) and S_{03} (blue line). Note that $S_{02} = S_{01}$ due to the symmetry of trial ansatz and the Hamiltonian. We can deduce that the system starts as a product state $\rho_{\mathrm{in}} = \rho_{03} \otimes \rho_{12}$ since $S_{03} = 0$ at the start (indeed, we also find that both density matrices have $rank = 1$ as expected). Additionally, we see that the initial state is not extremely entangled since $S_{01} \approx 1/2$ while for a maximally entangled state it would have been 2. The time evolution initially builds up correlations between the pair of qubits (0,3) and the pair (1,2) as can be seen by the growing entropies along all inequivalent bipartitions and eventually leads again to a product state similar to the initial one but with much larger entanglement. Indeed, around time $t \sim 0.45$, both the single qubit entropies and the entropy S_{01} are close to their maximum value. To understand better these correlations we also compute the concurrence [60] for the three partitions in pairs C_{01}, C_{02}, C_{03} (as before, the first two are the same by symmetry). This measure of entanglement is defined for a 2 qubit density matrix ρ as

$$C(\rho) = \max\{0, \lambda_0 - \lambda_1 - \lambda_2 - \lambda_3\}, \tag{44}$$

where λ_i are the square roots of the eigenvalues, in decreasing order, of the non-Hermitian matrix

$$M = \rho(Y \otimes Y)\rho^*(Y \otimes Y) \tag{45}$$

and the star indicates complex conjugation. The usefulness of this measure is its relation with the entanglement of formation [60,61], which is the minimum number of maximally entangled pairs needed to represent ρ with an ensemble of pure states [61]. In particular, the two quantities are related through the following result from Wootters [60]:

$$E_F(\rho) = h\left(\frac{1 + \sqrt{1 - C(\rho)^2}}{2}\right), \tag{46}$$

where

$$h(x) = -x\log_2(x) - (1 - x)\log_2(1 - x) \tag{47}$$

and we see that E_F is monotonically increasing with the concurrence $0 \le C \le 1$.

Interestingly, we find $C_{01} = C_{02} = 0$ indicating that these two qubit mixed states (indeed, S_{01} is never zero here) do not require any entanglement to be produced (i.e., the entanglement of formation is zero). The concurrence of the state ρ_{03} is instead relatively large and reaches close to the value for maximally entangled states at the same position where the entropies have the maximum.

The bottom panel shows the ratio of runs that looked decohered, and we can see that there is a correlation between a large decoherence rate and a large entanglement. A more detailed understanding of the relation between entanglement of formation and the fidelity of state preparation on non-error-corrected quantum architecture will be the subject of future work.

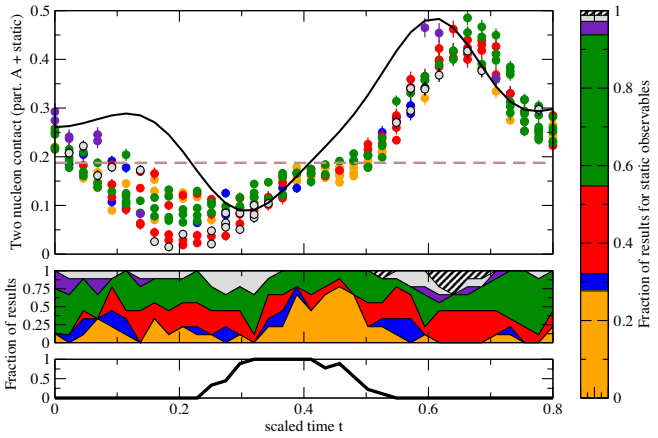

FIG. 9. Extrapolation procedures used to mitigate errors in the results for the two-body contact P_{dyn} defined in Eq. (40) of the main text. The rightmost vertical panel and the bottom horizontal panel are the same as in Fig. 8 and reported here for reference.

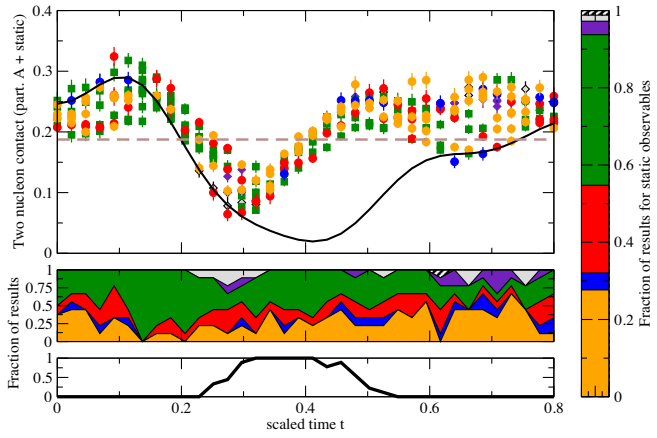

FIG. 10. Extrapolation procedures used to mitigate errors in the results for the two-body contact P_{dyn} defined in Eq. (41) of the main text. The rightmost vertical panel and the bottom horizontal panel are the same as in Fig. 8 and reported here for reference.

IV. CONCLUSIONS AND OUTLOOK

In this paper we have attempted a first qualitative estimate of the quantum computing resources required for a minimally realistic study of neutrino-nucleus interactions. The number of qubits required and gate counts are presented as a function of the number of nucleons and the target energy resolution in the hadronic final state. These estimates neglect completely the overhead caused by active error correction, and therefore should be considered as lower bounds on the physical resources needed for a successful execution with controllable error.

Because of the presence of substantial noise sources, full-scale studies using realistic models of nuclei and their interactions are not yet feasible with today's hardware, but showcase an important potential application of quantum computers.

We also present results for a simple problem using present-day quantum hardware, implementing both variational algorithms for the preparation of the nuclear ground state and product formulas for the time evolution operator also required for calculating the response. Error mitigation strategies are presented and their beneficial impact on computation of current day machines assessed. As can be seen clearly from the results presented in Figs. 8, 9, and 10, unitary errors can be particularly large and a more efficient strategy than what was presented here is needed to alleviate them (e.g., using Pauli twirling [55]). Another interesting outcome of our analysis of the hardware results is strong correlation between the entanglement of formation of the state being prepared and the amount of depolarizing noise that this is subject to (see Fig. 11 and the discussion on it). This behavior is not necessarily expected for computations not using active error correction, and we plan to further explore this issue in the future.

Nevertheless, even these simple models, with simplified interactions and a small number of nucleons, allow one to begin to understand important issues such as the importance of quantum interference in the cross sections and the expected quantum to classical transition in the examination of explicit final states, currently handled by quasiclassical generators.

Further studies of the linear response and the final states are required to understand the impact of quantum computers on accelerator neutrino and related experiments. We can foresee that quantum computers will play

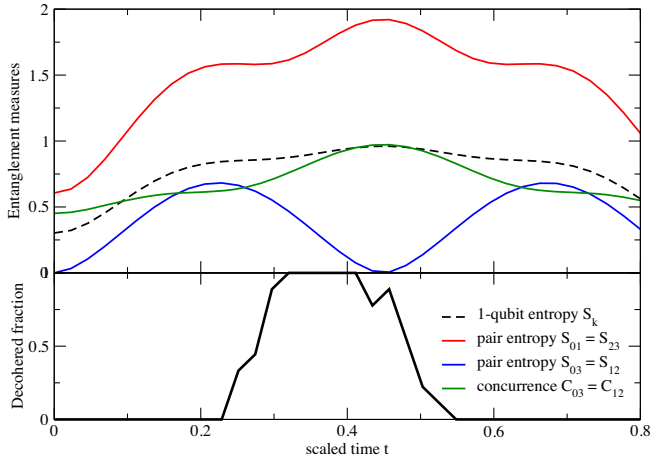

FIG. 11. The top panel shows, as a function of time, different measures of entanglement obtained analytically from the expected results. The black dashed line shows the single qubit entanglement entropy, the red (blue) solid line corresponds to the entanglement entropy of the pair of qubits 01 (03), and the solid green curve is the concurrence for the pair of qubits (03). For the pair 01 the concurrence is identically zero at all times. The bottom panel shows the fraction of runs where decoherence has been detected (same as in Fig. 8).

a significant role as their capabilities in the number of qubits and error reduction advance. We expect the quantum linear response to be an early application of quantum computers, and neutrino scattering off nuclei to be a particularly important one.

ACKNOWLEDGMENTS

\We thank S. Pastore, A. Lovato, N. Rocco, and R. Schiavilla for discussions on neutrino-nucleus scattering, and A. Baroni for discussions on implementing nuclear models with quantum computers. In addition, we acknowledge use of the IBM Q for this work. The views expressed are those of the authors and do not reflect the official policy or position of IBM or the IBM Q team. This research used resources of the Oak Ridge Leadership Computing Facility, which is a DOE Office of Science User Facility supported under Contract No. DE-AC05-00OR22725. This project was funded in part by the DOE HEP QuantISED Grant No. KA2401032. This manuscript has been authored by Fermi Research Alliance, LLC under Contract No. DE-AC02-07CH11359 with the U.S. Department of Energy, Office of Science, Office of High Energy Physics. The work of A. R. was supported by the U.S. Department of Energy, Office of Science, Office of Advanced Scientific Computing Research (ASCR) quantum algorithm teams program, under field work proposal No. ERKJ333 and by the Institute for Nuclear Theory under U.S. Department of Energy Grant No. DE-FG02-00ER41132.

APPENDIX A: SIMPLE CIRCUIT PRIMITIVES

We provide, for completeness, a few circuit representations of unitary operators we use throughout our work. The first three are exponentials of Pauli operators for which three basic gates are needed:

(i) one-body contributions

$$e^{-i\delta\beta Z_i} \equiv e^{-i\tilde{\beta} Z_i} \equiv \tag{A1}$$

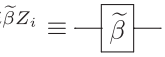

(ii) two-body contributions

$$e^{-i\delta\gamma Z_i Z_j} \equiv e^{-i\tilde{\gamma} Z_i Z_j} \equiv \tag{A2}$$

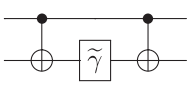

(iii) three-body contributions

$$e^{-i\delta t\eta Z_i Z_j Z_k} \equiv e^{-i\tilde{\eta} Z_i Z_j Z_k} \equiv \tag{A3}$$

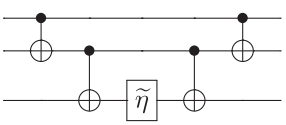

Another primitive we use is the rotation around the Z axis controlled by an ancilla (see, e.g., [62])

$$= \tag{A4}$$

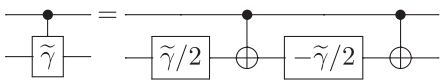

This implementation requires 2 CNOT and 2 rotations for every controlled rotation.

APPENDIX B: DETAILS ON TROTTERIZATION

In this appendix, we provide the detailed derivation of the Trotterization discussed in Sec. II A. We estimate the numbers of Trotter steps and the gate costs required for different Hamiltonian splittings and orders of the Trotter-Suzuki expansion.

To facilitate further discussion, we will consider two easy to compute upper bounds for operator norms $\|O\|$ of some Hermitian operator $O = \sum_j \beta_j P_j$ written as an expansion over (tensor products of) Pauli matrices P_j:

(i) absolute value norm

$$\|O\|_{\text{abs}} = \left\| \sum_j \beta_j P_j \right\| \text{abs} = \sum_j \|\beta_j P_j\| = \sum_j |\beta_j| \tag{B1}$$

(ii) physical norm

$$\|O\|_{\text{phys}} = \sup\{\|O|\psi\rangle\| : |\psi\rangle \text{ physical state}\}, \tag{B2}$$

where for vectors we use the 2-norm. In this context an example of a physical vector is an eigenstate of the total number operator with eigenvalue A.

For instance, if we consider the potential energy operator, we see that the absolute norm scales linearly with the lattice dimension

$$\|V\|_{\text{abs}} = M(6|C_0| + 8|D_0|). \tag{B3}$$

On the other hand, because of the fact that our interactions are contact terms, particles can interact with each other only when they are at the same lattice point and the absolute norm above will greatly overestimate the potential contribution for a physical state with A fermions distributed among the $N_f = 4$ types. For a physical state the maximum value of the three-body potential is reached when we occupy a lattice site with four particles, which means

$$\|V_3\|_{\text{phys}} \leq 4|D_0| \left\lfloor \frac{A}{4} \right\rfloor \leq A|D_0|, \tag{B4}$$

where $\lfloor x \rfloor$ is the floor function. For the two-body interaction we can have either two, three, or four particles per site resulting in

$$\|V_2\|_{\text{phys}} \leq |C_0| \max\left\{ \left\lfloor \frac{A}{2} \right\rfloor, 3\left\lfloor \frac{A}{3} \right\rfloor, 6\left\lfloor \frac{A}{4} \right\rfloor \right\}. \tag{B5}$$

In the physically relevant case $M \gg A$, the physical norm will be much smaller than the absolute one. For the kinetic energy we have instead

$$\|K\|_{\text{abs}} = N_K \left|\frac{t}{2}\right| = 2DMN_f|t|, \tag{B6}$$

while for physical states we find instead

$$\|K\|_{\text{phys}} \leq AD\frac{\hbar^2}{2m}k_{\text{max}}^2 = ADt\pi^2, \tag{B7}$$

where $k_{\text{max}} = \pi/a$ is the largest momentum in the box. Finally, as we did in Eq. (12), we can use these results to place a physical upper bound on the maximum spread in energy attainable in an A-body system as

$$\begin{aligned}\Delta H &= E_{\text{max}} - E_{\text{min}} \\ &= \|K\|_{\text{phys}} + \|V_2\|_{\text{phys}} + \|V_3\|_{\text{phys}} + Ab_{\text{max}},\end{aligned} \tag{B8}$$

where b_{max} is the nuclear binding energy at saturation and we have used the estimate $|E_{\text{min}}| \leq Ab_{\text{max}}$ for the lowest energy value. A much better bound on the potential can be obtained by realizing that the two potential terms have opposite signs and their contributions will partially cancel; this implies that we can use

$$\|V\|_{\text{phys}} = \max\{n_2, n_3, n_4\} < \|V_2\|_{\text{phys}} + \|V_3\|_{\text{phys}}, \tag{B9}$$

where we have defined

(i) $n_2 = |C_0|\lfloor\frac{A}{2}\rfloor$
(ii) $n_3 = |D_0 + 3C_0|\lfloor\frac{A}{3}\rfloor$
(iii) $n_4 = |4D_0 + 6C_0|\lfloor\frac{A}{4}\rfloor$

As motivated in the main text, we will use physical norms $\|\cdot\|_{\text{phys}}$ whenever possible to bound, and in the following we will remove the subscript when this causes no confusion.

1. Product formulas: Analytical bounds

We can now start the discussion about product formulas derived from the Trotter-Suzuki expansion for the time evolution operator. At first order, we find the simple decompositions (13) and (14) presented in the main text

$$U_L^{\alpha}(\tau) = \prod_k^{N_K} e^{-i\tau K_k} e^{-i\tau V} \tag{B10}$$

for the α splitting and

$$U_L^{\beta}(\tau) = e^{-i\tau K} e^{-i\tau V} \tag{B11}$$

for the β splitting. Following the same derivation presented in [38] (see also Sec. VB of [56] for more details), we find

$$\|e^{-i\tau H} - U_L^{\alpha/\beta}(\tau)\| \leq (\tau\Lambda_{\alpha/\beta})^2 \exp(\tau\Lambda_{\alpha/\beta}), \tag{B12}$$

where $\Lambda_{\alpha/\beta}$ is an upper bound for the sum of norms of the individual terms in the Hamiltonian expansions. In particular, we have

$$\Lambda_\alpha = \sum_k \|K_k\| + \|V\| = |t|N_K + \|V\|, \tag{B13}$$

$$\Lambda_\beta = \|K\| + \|V\|. \tag{B14}$$

At this point, we first note that we can interpret the evolution under the approximate propagator $U_L(\tau)$ as an exact time evolution under the effective Hamiltonian (cf. [63]) given by

$$H_{\text{eff}}^{\alpha/\beta}(L) = \frac{\ln(U_L^{\alpha/\beta}(\tau))}{-i\tau}, \tag{B15}$$

and for small values of τ, we estimate the error in the energy eigenvalues using (see also [33] for a tighter bound)

$$\|H - H_{\text{eff}}^{\alpha/\beta}(L)\| = \frac{1}{\tau}\|e^{-i\tau H} - U_L^{\alpha/\beta}(\tau)\|. \tag{B16}$$

To control the approximation error introduced by using the approximate evolution operator U_L, we can split the time interval τ required by our algorithm into r steps and consider instead

$$\|e^{-i\tau H} - U_L^{\alpha/\beta}(\tau/r)^r\| = \delta_\tau, \tag{B17}$$

leading to an energy error ϵ_τ bounded by

$$\frac{\delta_\tau}{\tau} \leq \frac{\tau}{r}\Lambda_{\alpha/\beta}^2 \exp\left(\frac{\tau\Lambda_{\alpha/\beta}}{r}\right). \tag{B18}$$

Following the same analysis presented in [38], we obtain the following analytical bound for the number of Trotter steps needed for time τ:

$$r_{1;A} = \left\lceil \max\left\{\tau\Lambda_{\alpha/\beta}, \frac{e\tau\Lambda_{\alpha/\beta}^2}{\epsilon_\tau}\right\}\right\rceil. \tag{B19}$$

In Fig. 12 we present the expected number of steps needed to perform time evolution for both the base time $\tau_{\text{base}} = 2\pi/\Delta H$ (black and green lines) and the whole sequence of W evolutions for a total time of $\tau_{\text{tot}} = (2^W - 1) * \tau_{\text{base}}$ (red and blue lines) where the number of ancilla qubits W is obtained for a fixed resolution $\Delta\omega$ [cf. Eq. (18) in the main text]. Results are presented for the hardest interaction ($a = 1.4$ fm) and for two different target resolutions: $\delta\omega = 100$ MeV (solid lines) and $\Delta\omega = 10$ MeV (dashed lines). In both cases, we fix the energy error ϵ_τ to be half the resolution.

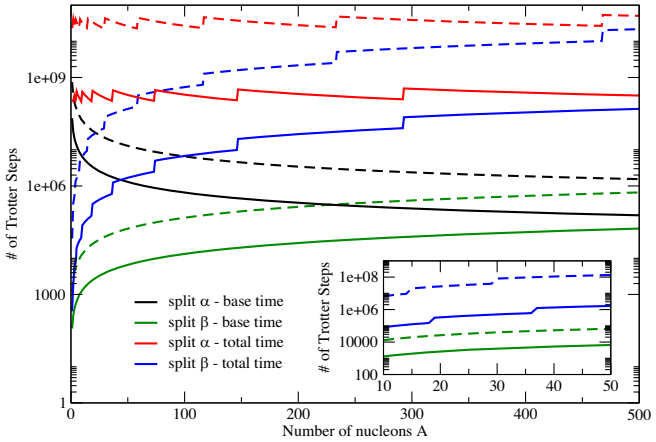

FIG. 12. Estimated number of Trotter steps for both splittings of the Hamiltonian and two different target resolutions: $\delta\omega = 100$ MeV (solid lines) and $\delta\omega = 10$ MeV (dashed lines). The inset shows results for the best performing splitting (the β one) in the region of the mass number of interest for neutrinos.

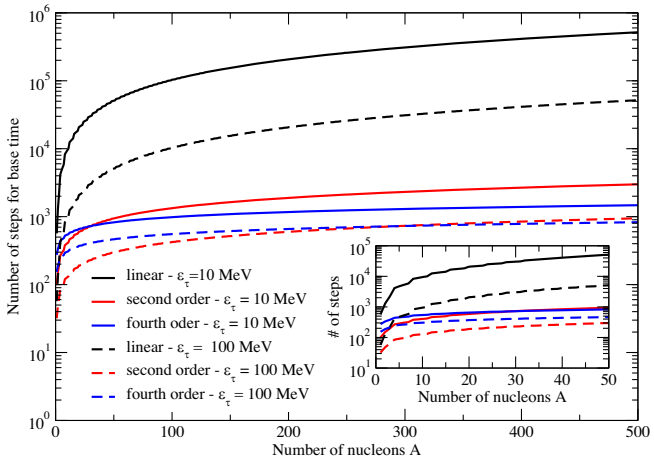

FIG. 13. Number of Trotter steps required for a target precision $\epsilon_\tau = 10$ MeV (100 MeV) using β splitting shown as solid (dashed) lines for the base time $\tau = 2\pi/\Delta H$.

Higher order decompositions allow for a reduction of the scaling of the approximation error with the evolution time and can therefore provide an important efficiency gain. Here we will consider the even order Trotter-Suzuki formulas [40] defined by the recursion

$$S_{2k}(\tau) = [S_{2k-2}(\tau_k)]^2 S_{2k-2}(\tau - 4\tau_k)[S_{2k-2}(\tau_k)]^2 \quad \text{(B20)}$$

with

$$S_2(\tau) = \prod_{k=1}^{N_K} e^{-i\frac{\tau}{2}K_k} e^{-i\frac{\tau}{2}V} e^{-i\frac{\tau}{2}V} \prod_{k=N_K}^{1} e^{-i\frac{\tau}{2}K_k} \quad \text{(B21)}$$

and $\tau_k = \tau/(4 - 4^{1/(2k-1)})$ for $k > 1$. Using these approximations (cf. [38,56]) to the evolution operator the number of steps needed for a given accuracy becomes bounded by

$$r_{2k;A} = \left\lceil \rho_{2k} \max\left\{1, \left(\frac{2e\Lambda 5^{k-1}}{3\epsilon_\tau}\right)^{\frac{1}{2k}}\right\}\right\rceil \quad \text{(B22)}$$

with $\rho_{2k} = 2\tau 5^{k-1}\Lambda$.

As reported in the main text, the explicit expressions for the second order formulas with both kinds of breakup are

$$S_\alpha(\tau) = e^{-i\frac{\tau}{2}V} \prod_{k=1}^{N_K} e^{-i\frac{\tau}{2}K_k} \prod_{k=N_K}^{1} e^{-i\frac{\tau}{2}K_k} e^{-i\frac{\tau}{2}V} \quad \text{(B23)}$$

for the α splitting, while for the β splitting we consider the two options

$$S_\beta^{K+V}(\tau) = e^{-i\frac{\tau}{2}K} e^{-i\tau V} e^{-i\frac{\tau}{2}K} \quad \text{(B24)}$$

and

$$S_\beta^{V+K}(\tau) = e^{-i\frac{\tau}{2}V} e^{-i\tau K} e^{-i\frac{\tau}{2}V}. \quad \text{(B25)}$$

These formulas are used to produce the results reported next.

In Fig. 13, we show results for $r_{1;A}$, $r_{2;A}$, and $r_{4;A}$ for the base time interval needed for β splitting with $\tau = 2\pi/\Delta H$ using the hardest interaction with $a = 1.4$ fm (softer interactions require a smaller number of steps due to the smaller norm of the Hamiltonian). The second order formulas (red lines) show a clear advantage over the linear decompositions (black lines). On the other hand, the fourth order formulas (blue lines) become favorable only when tackling big enough problems. Specifically, the breakeven point is $A = 24$ ($A = 234$) for higher target accuracy $\delta\omega = 10$ MeV (lower target accuracy $\delta\omega = 100$ MeV).

During the phase estimation stage of our algorithm, we need to perform (controlled) time evolution for a set of $N_{\text{tot}} = 2^{W-1} = \Delta H/\epsilon_\tau$ (note the factor of 2 coming from $\epsilon_\tau = \Delta\omega/2$) time intervals given by $T_k = 2^k\tau$ for $k \in [0, W-1]$. One way to achieve this is to decompose optimally the unitary operator $U_L(\tau)$ using the bounds presented above and simply repeat this basic one as needed. The resulting total number of steps required by this algorithm is denoted as "same r" in Fig. 14. An alternative approach is to adaptively decompose each of the N_{tot} evolution unitary operators individually and then sum the number of steps together. This method produces the results denoted as "adaptive r" in Fig. 14 and, as expected, is usually more efficient than the simpler standard one. This is the strategy used throughout the main text.

2. Product formulas: Commutator bounds

As mentioned in Sec. II A, the errors in product formulas should depend on the commutators of the terms in the Hamiltonian and not directly on their norms; this is one of the deficiencies of the bounds considered above and

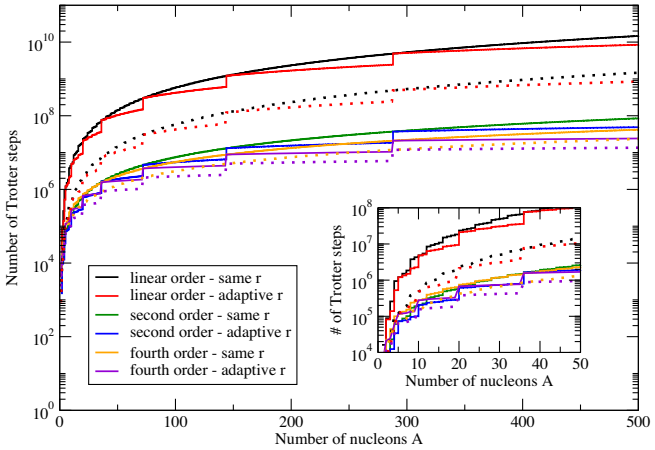

FIG. 14. Total number of Trotter steps required for a target precision $\epsilon_\tau = 10$ MeV (100 MeV) shown as solid (dotted) lines. In contrast to Fig. 13 these results are obtained for the full propagation time $T = 2^{W-1}\tau$. See text for details.

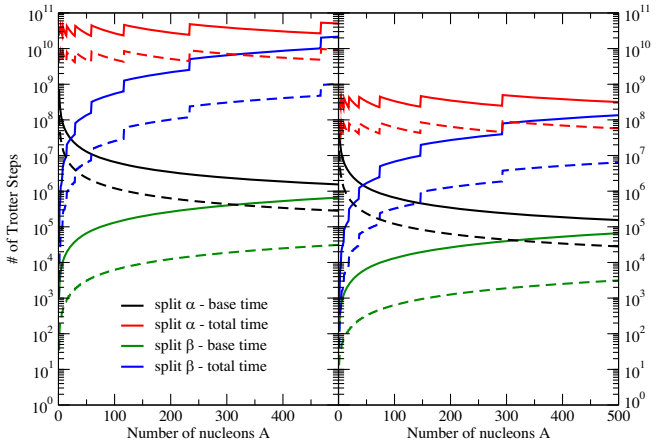

FIG. 15. Comparison of the analytical vs commutator bounds $r_{1:A}$ and $r_{1:C}$ for the linear Trotter-Suzuki breakup with both splitting schemes. The left panel corresponds to a target resolution $\Delta\omega = 10$ MeV while the right panel corresponds to $\Delta\omega = 100$ MeV.

prevents them from being tight. For the linear Trotter decomposition, we can consider the commutator bound similar to the one from [38]

$$\|e^{-i\tau H} - U_L^{\alpha/\beta}(\tau)\| \leq \frac{C_{\alpha/\beta}}{2}\tau^2 + \frac{(\tau\Lambda_{\alpha/\beta})^3}{3}\exp(\tau\Lambda_{\alpha/\beta}), \tag{B26}$$

where

$$\begin{aligned} C_\alpha &= \|\sum_{j>k}[H_k, H_j]\| = \|\sum_k^{N_K}[K_k, V] + \sum_{j>k}[K_k, K_j]\| \\ &\leq 2N_K|t|\|V\|_{\text{phys}} + N_K(N_K-1)t^2 \leq \Lambda_\alpha^2 \end{aligned} \tag{B27}$$

for the α splitting, and for the β splitting

$$C_\beta = \|[K, V]\| \leq 2\|K\|_{\text{phys}}\|V\|_{\text{phys}} \leq \Lambda_\beta^2. \tag{B28}$$

We can now estimate the number of intervals r by defining

$$r_{1;C} = \min\{r \in \mathbb{N} : \Gamma^1_{\alpha/\beta}(r) \leq \epsilon_\tau\}, \tag{B29}$$

where $\Gamma^1_{\alpha/\beta}$ is the error estimator obtained from the upper bound Eq. (B26) above,

$$\Gamma^1_{\alpha/\beta}(r) = \frac{C_{\alpha/\beta}}{2}\frac{\tau}{r} + \left(\frac{\tau}{r}\right)^2\frac{(\Lambda_{\alpha/\beta})^3}{3}\exp\left(\frac{\tau}{r}\Lambda_{\alpha/\beta}\right), \tag{B30}$$

and for $C_{\alpha/\beta}$ we use their upper bounds derived above.

The importance of including information about the commutators is apparent from the results in Fig. 15 where we show the improved bounds $r_{1;C}$ (dashed lines) together with the analytical results $r_{1;A}$ (solid lines) for the two target precisions separately (the left panel corresponds to $\Delta\omega = 10$ MeV while the right panel corresponds to $\Delta\omega = 100$ MeV). The adoption of the commutator bounds provides an improvement of the same order of magnitude as going to a second order expansion (cf. Fig. 1 in the main text).

For the second order expansion instead we use the result of [33] to construct the estimators

$$r_{2;C} = \min\{r \in \mathbb{N} : \Gamma^2_{\alpha/\beta}(r) \leq \epsilon_\tau\}, \tag{B31}$$

where the error estimators are given by

$$\Gamma^2_{\alpha/\beta}(r) = \frac{1}{12}\left(\frac{\tau}{r}\right)^2 T_{\alpha/\beta}, \tag{B32}$$

with

$$\begin{aligned} T_\alpha &= \sum_{j,k}^{N_K}\|[[V, K_j], K_k]\| + \sum_j^{N_K}\|[[V, K_j], V]\| \\ &\quad + \sum_i^{N_K}\sum_{j>i}\sum_{k>i}\|[[K_i, K_j], K_k]\| \\ &\quad + \sum_i^{N_K}\sum_{j>i}^{N_K}\|[[K_i, K_j], K_i]\| \\ &\leq 4N_K^2t^2\|V\|_{\text{phys}} + 4N_K|t|\|V\|^2_{\text{phys}} + 2N_K(N_K-1)|t|^3 \\ &\quad + \frac{2}{3}N_K(2N_K^2 - 3N_K + 1)|t|^3 \end{aligned} \tag{B33}$$

and two different expressions for splitting β depend on the ordering of the operators

$$T_\beta^{K+V} = \|[[K,V],V]\| + \frac{1}{2}\|[[K,V],K]\| \leq 2\|K\|_{\text{phys}}\|V\|_{\text{phys}}(2\|V\|_{\text{phys}} + \|K\|_{\text{phys}}) \quad \text{(B34)}$$

and

$$T_\beta^{V+K} = \|[[V,K],K]\| + \frac{1}{2}\|[[V,K],V]\| \leq 2\|K\|_{\text{phys}}\|V\|_{\text{phys}}(2\|K\|_{\text{phys}} + \|V\|_{\text{phys}}). \quad \text{(B35)}$$

We show the resulting estimates for $r_{2;C}$ at a fixed target accuracy $\Delta\omega = 100$ MeV for the two splitting methods in Fig. 2 on the main text.

3. Product formulas: Gate cost per step

To implement the time-evolution unitary operators described in the preceding section, we need to implement three independent unitary operators

$$U_1(\tau) = e^{-i\tau V}, \quad \text{(B36)}$$

$$U_2(\tau) = e^{-i\tau K}, \quad \text{(B37)}$$

$$U_3(\tau) = \prod_{k=1}^{N_K} e^{-i\tau K_k}, \quad \text{(B38)}$$

$$U_4(\tau) = \prod_{k=N_K}^{1} e^{-i\tau K_k} = U_3^\dagger(-\tau), \quad \text{(B39)}$$

from which we construct

$$U_L^\alpha(\tau) = U_3(\tau)U_1(\tau), \quad \text{(B40)}$$

$$U_L^\beta(\tau) = U_2(\tau)U_1(\tau), \quad \text{(B41)}$$

$$S_\alpha(\tau) = U_1\left(\frac{\tau}{2}\right)U_3\left(\frac{\tau}{2}\right)U_4\left(\frac{\tau}{2}\right)U_1\left(\frac{\tau}{2}\right), \quad \text{(B42)}$$

$$S_\beta^{K+V}(\tau) = U_2\left(\frac{\tau}{2}\right)U_1(\tau)U_2\left(\frac{\tau}{2}\right), \quad \text{(B43)}$$

$$S_\beta^{V+K}(\tau) = U_1\left(\frac{\tau}{2}\right)U_2(\tau)U_1\left(\frac{\tau}{2}\right). \quad \text{(B44)}$$

a. Evolution operator for the interaction term

Since the interactions in our model have zero range, all the M distinct potential energy operators acting on different sites will commute,

$$U_1(\tau) = e^{-i\tau V} = \prod_{i=1}^{M} e^{-i\tau V_i} \quad \text{(B45)}$$

with V_i acting nontrivially on only N_f qubits at a time. This implies that we need to worry about the implementation of only a single diagonal Hamiltonian term of the following form:

$$V_i = \alpha + \beta\sum_{f=0}^{3} Z_f + \gamma\sum_{f>f'}^{3} Z_f Z_{f'} + \eta\sum_{f>f'>f''}^{3} Z_f Z_{f'} Z_{f''}, \quad \text{(B46)}$$

where the coefficient can be read directly from the general expression in Eq. (7). Using well-known general decompositions for exponentials of Pauli matrices discussed in Appendix A, we can express the evolution operator $U_i(\delta) = \exp(-i\delta V_i)$ in terms of single qubit Z rotations and CNOT gates. Assuming all-to-all connectivity within the 4 qubit cell (and with the possible controlling ancilla), a straightforward implementation using the above-mentioned gadgets will require 14 rotations and 28 CNOT for the uncontrolled version and 28 rotations and 56 CNOT for the controlled unitary evolution. We know, however, that the optimal circuit to implement an arbitrary diagonal unitary on n qubits requires at most $2^{n+1} - 3$ one and two qubit gates (see [32,64]). Given the lack of a four-body contact interaction, and assuming all-to-all connectivity, for our model this expansion produces the following circuit with depth 28 (14 rotations + 14 CNOT):

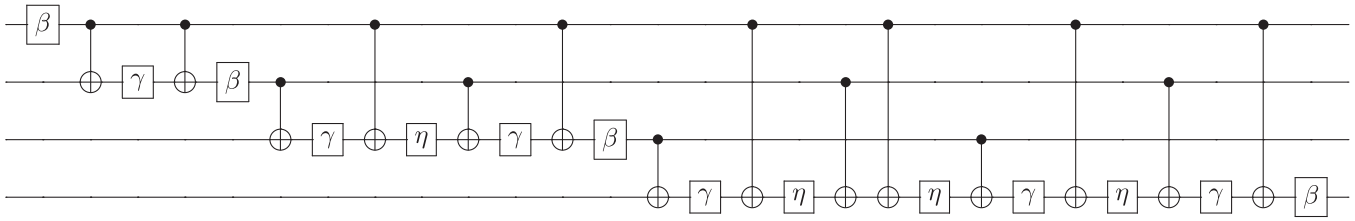

where the one qubit gates are appropriate Z rotations [cf. Eq. (B46)]. Under the more stringent constraint of 2D planar connectivity one can optimize the construction for parallel efficiency, and the result of this exercise (first reported in [65]) is the following circuit:

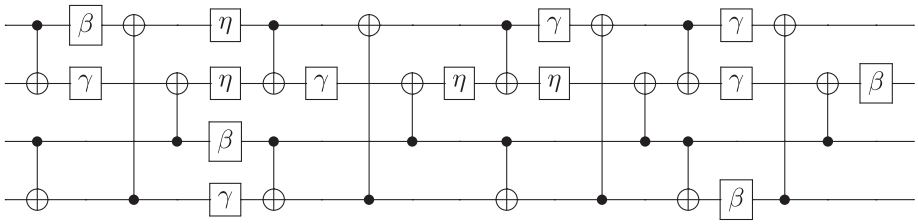

(B47)

which has serial (parallel) depth of 30 (15) with a 2D nearest neighbor connectivity (7 rotations + 8 CNOT in parallel). The gate cost of implementing the potential energy propagator is summarized in Table III.

b. Evolution operator for the hopping term

We will, for now, only assume linear connectivity for our implementation of the last three evolution operators. The exact propagator for hopping term $U_2(\tau)$ can be obtained using either the FFFT whenever $4M$ is power of 2 or else the Givens rotations described in [33,43]. In the latter case, due to our choice of ordering where single particle states on the same lattice point and different spin-isospin are next to each other (this is for ease of implementation of the potential energy part, especially the triples), we consider the system as $4M$ spinless fermions and use all the $2M(4M-1)$ Givens rotations each requiring two rotations (which can be performed in parallel) and 5 CNOT for a total of $4M(4M-1)$ arbitrary Z rotations and $10M(4M-1)$ CNOT with parallel depth $8M-3$ (using results from [43]). This circuit must be executed twice and a final set of $4M$ rotations in depth 1 must be performed in between. Luckily, only these need to be controlled when performing the controlled time evolution. The gate cost of implementing the propagator U_2 is summarized in Table IV.

We turn now to the implementation of U_3, a naive implementation of all the N_K terms separately would require two rotations (by the same angle), 8 Hadamard and 4 S gates and $4(p_k-q_k)$ CNOT for each term

$$e^{-i\tau K_k} = e^{-i\frac{\tau}{2}(X_{p_k}X_{q_k}+Y_{p_k}Y_{q_k})Z_{p_k+1}\cdots Z_{q_k-1}} \tag{B48}$$

in the expansion of $U_3(\tau)$, where the string of Pauli Z comes from the Jordan-Wigner mapping. This estimate comes from the following explicit construction (cf. [63]):

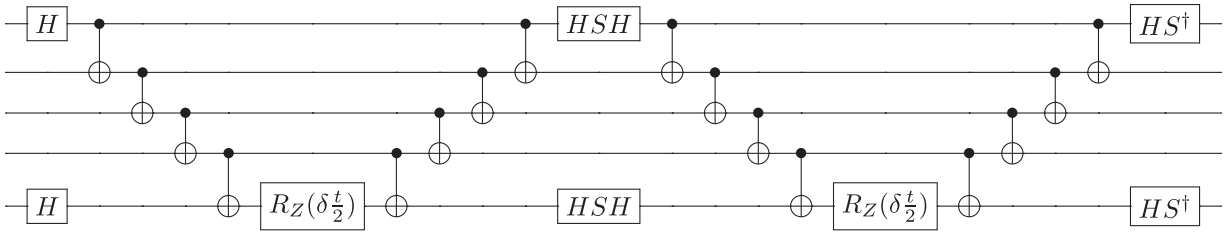

(B49)

where the first is the qubit corresponding to single orbital p and the last one is q. This can be further reduced if arbitrary connectivity is allowed (see, e.g., [35]). In total, one finds at most $24M$ rotations and less than $48M^2$ nearest neighbor CNOT gates. The same estimates also hold for U_4. Using the fermionic-swap network algorithm instead, we can implement U_3 and U_4 by performing $2M(4M-1)$ two-qubit fermionic simulation gates with parallel depth $4M$,

TABLE III. Gate cost for the potential energy propagator.

	# c-Rz		# CNOT	
	Serial	Parallel	Serial	Parallel
Naive	14M	14	28M	28
Serial optimized	14M	14	14M	14
Parallel optimized	14M	7	16M	8

TABLE IV. Gate cost for the U_2 propagator.

	# Rz		# c-Rz		# CNOT	
	Serial	Parallel	Serial	Parallel	Serial	Parallel
U_2	$32M^2$	16M-4	0	0	20M(4M-1)	80M-28
c-U_2	8M(4M-1)	16M-6	4M	1	4M(20M-3)	80M-30

TABLE V. Gate cost for the U_3/U_4 propagator. See also Fig. 16 for tighter estimates of the naive cost.

	# c-Rz		# CNOT	
	Serial	Parallel	Serial	Parallel
Naive	<24M	<24M	$<48M^2$	$<48M^2$
Fermionic swap	<24M	8M	6M(4M-1)	12M

each one requiring at most 5 rotations and 3 CNOT (since we are not implementing evolution under the on site interaction at the same time, this reduces to just 2 arbitrary rotations [66]). Most of these are simple fermionic swap gates

$$\mathrm{fSWAP} = \begin{pmatrix} 1 & 0 & 0 & 0 \\ 0 & 0 & 1 & 0 \\ 0 & 1 & 0 & 0 \\ 0 & 0 & 0 & -1 \end{pmatrix}, \tag{B50}$$

requiring 3 CNOT and additional Clifford gates. The number of (controlled) arbitrary rotations is therefore at most equal to the serial count for the naive implementation or $8M$ in the parallel case. The gate cost of implementing the propagators U_3 and U_4 is summarized in Table V.

In Fig. 16 we present the empirical gate counts for the evolution operator U_3/U_4 using both the naive implementation, the fermionic swap network and the exact implementation using Givens rotations (for the latter one we count half the cost of noncontrolled rotations). We see that the latter two approaches provide a considerable reduction in CNOT counts but at the price of raising the parallel depth for the rotation gates, this might have an impact on the fault-tolerant implementation of the algorithm.

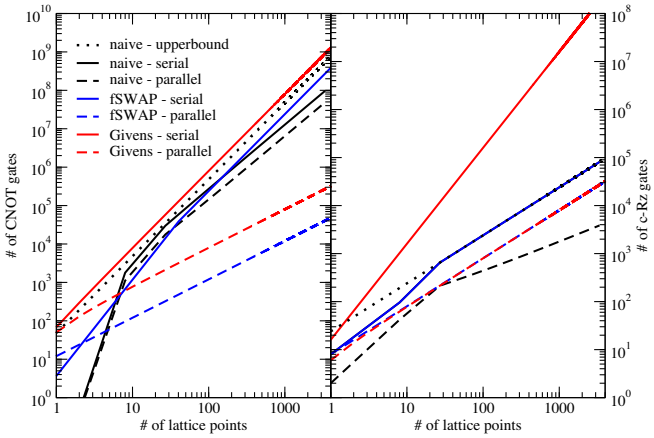

FIG. 16. Empirical gate counts from a simulation of the naive implementation of U_3/U_4 for system sizes $M \in (8, 3375)$. Also shown are the gate cost estimates for the fSWAP algorithm and the implementation of U_2 using Givens rotations (cf. Table V).

APPENDIX C: DETAILS ON QUBITIZATION

The basic idea behind qubitization [34] is to represent the system Hamiltonian in the following way:

$$H = \lambda(\langle G| \otimes \mathbb{1})\mathrm{select}(H)(\mathbb{1} \otimes |G\rangle), \tag{C1}$$

where the first register holds an ancilla space of dimension $> \Gamma$ where

$$H = \sum_{j=0}^{\Gamma-1} \lambda_j H_j, \tag{C2}$$

the coefficients $\lambda_j > 0$ and H_j are Clifford operations. For ease of derivation, we will assume that $H_0 \equiv \mathbb{1}$ and if the original Hamiltonian was traceless, we add it while increasing Γ accordingly. The two main subroutines we need to perform qubitization are the *select* unitary V_S and the *prepare* unitary V_P which can be respectively defined as

$$V_S = \sum_{j=0}^{\Gamma-1} |j\rangle\langle j| \otimes H_j \tag{C3}$$

and

$$V_P|0\rangle|G\rangle = \frac{1}{\sqrt{\lambda}} \sum_{j=0}^{\Gamma-1} \sqrt{\lambda_j}\,|j\rangle \qquad \lambda = \sum_{j=0}^{\Gamma-1} \lambda_j. \tag{C4}$$

As mentioned in the main text, the central object of this scheme is the qubiterate unitary defined in Eq. (19) of the main text and which can be implemented using the two basic unitaries defined above as

$$Q = -i((2|G\rangle\langle G| - \mathbb{1}) \otimes \mathbb{1})V_S, \tag{C5}$$

whose eigenvalues are

$$\eta_\pm = \mp\, e^{\pm i \arcsin(\eta)}, \tag{C6}$$

where $H/\lambda = \sum_\eta \eta|\eta\rangle\langle\eta|$ is the spectral decomposition of the (scaled) Hamiltonian. The eigenvectors of the qubiterate are

$$|\eta_\pm\rangle = \frac{1}{\sqrt{2}}(|G_\eta\rangle \pm i|G_\eta^\perp\rangle), \tag{C7}$$

which are connected with the energy eigenstate by

$$|G_\eta\rangle = |G\rangle \otimes |\eta\rangle \tag{C8}$$

and

$$|G_\eta^\perp\rangle = \frac{\eta|G_\eta\rangle - \mathrm{select}(H)|G_\eta\rangle}{\sqrt{1-\eta^2}}. \tag{C9}$$

1. Gate cost of the qubiterate

We now proceed to estimate the qubiterate gate cost. Following the discussion in the main text in order to implement the sequence of controlled qubiterates, we need to implement an initial controlled prepare (whose small cost we neglect in the estimates that follow), and then for every qubiterate we need one *select* and two *prepare* without controls and one controlled reflection. Since we are trying to provide a lower bound on the gate count and techniques that only need one copy of *prepare* per step are known [47], we will only count the cost of one prepare per step.

For our model with $N_f = 4$ fermionic species, the kinetic energy requires $\Gamma_K = 24M$ and the potential energy part needs $\Gamma_V = 14M$ for a total $\Gamma = 38M$. The size of the ancilla register required to encode the flag state $|G\rangle$ is thus $N_A = \lceil \log_2(\Gamma) \rceil$. The easiest unitary to implement is the *prepare* operation V_P defined by

$$V_P(|0\rangle) = |G\rangle = \frac{1}{\sqrt{\lambda}} \sum_{j=0}^{\Gamma-1} \sqrt{\lambda_j}\, |j\rangle. \tag{C10}$$

Without assuming any structure in the coefficients $\{\lambda_j\}$, we can always prepare the flag state $|G\rangle$ on the ancilla register with N_A qubits using at most (see, e.g., [67])

(i) $2^{N_A} - 2N_A - 2$ CNOT
(ii) $2^{N_A} - N_A - 2$ one qubit gates,

and to be conservative, we will count 3 z rotations per one-qubit unitary. The second unitary we need is the controlled reflection ${}_c\Pi_0$ acting on the N_A ancillas plus the control that we implement as in [38] using a multiply controlled Z gate with N_A controls implemented using the ancilla-based scheme described in [68], which needs

(i) $\lceil \frac{N_A-2}{2} \rceil$ ancillas in $|0\rangle$
(ii) $8N_A - 9$ T gates
(iii) $6N_A - 6$ CNOT gates
(iv) $4N_A - 6$ Hadamard gates

Finally we can implement the control circuit for the *select* operation V_S using the optimized scheme from [38] which needs $N_B = N_A - 1$ additional ancilla qubits prepared and returned in $|0\rangle$ and

(i) 2 NOT gates
(ii) $2^{N_A+1} + 2N_A - 8$ Hadamard gates
(iii) $2^{N_A-1} - N_A$ Phase gates
(iv) $152^{N_A-1} + 6N_A - 28$ $T/T^\dagger$ gates
(v) $152^{N_A-1} + 6N_A - 26$ CNOT gates

Note, however, that this control circuit will cycle over all the possible 2^{N_A} possible states of the control register and we can terminate this only after the needed Γ are obtained. To estimate this uncertainty of the analytical gate count, we will make use of the relation $2^{N_A} \geq \Gamma > 2^{N_A-1}$ to bound the gates cost.

On top of this, we need to implement all the Γ controlled unitaries that are, however, all Clifford operations. Here, we neglect them to estimate a lower bound of the gate cost, which is sufficient for the comparison between qubitization and Trotter decompositions. Counting only two-qubit Clifford gates and rotations or T gates, and reusing ancillas for both *select* and the reflection, we find the following cost estimate for a single application of the controlled qubiterate:

(i) $2N_A - 1$ ancilla qubits
(ii) $172^{N_A-1} + 10N_A - 34$ CNOT gates
(iii) $2^{N_A} - N_A - 2$ $U(2)$ gates
(iv) $152^{N_A-1} + 14N_A - 37$ $T/T^\dagger$ gates

The gate cost of qubitization is compared with that of Trotter decompositions in Fig. 3 in the main text. Note that T gates can be implemented using arbitrary Z rotations, and hence we count T gates as R_Z gates for the estimates there.

[1] Deep Underground Neutrino Experiment, http://www.dunescience.org (2019).
[2] O. Benhar, P. Huber, C. Mariani, and D. Meloni, Phys. Rep. **700**, 1 (2017).
[3] L. Alvarez-Ruso *et al.*, Prog. Part. Nucl. Phys. **100**, 1 (2018).
[4] C. Andreopoulos, A. Bell, D. Bhattacharya, F. Cavanna, J. Dobson *et al.*, Nucl. Instrum. Methods A **614**, 87 (2010).
[5] Y. Hayato, Nucl. Phys. B, Proc. Suppl. **112**, 171 (2002).
[6] T. Golan, C. Juszczak, and J. T. Sobczyk, Phys. Rev. C **86**, 015505 (2012).
[7] C. Juszczak, J. A. Nowak, and J. T. Sobczyk, Nucl. Phys. B, Proc. Suppl. **159**, 211 (2006).
[8] T. Golan, J. Sobczyk, and J. Zmuda, Nucl. Phys. B, Proc. Suppl. **229–232**, 499 (2012).
[9] O. Buss, T. Gaitanos, K. Gallmeister, H. van Hees, M. Kaskulov, O. Lalakulich, A.B. Larionov, T. Leitner, J. Weil, and U. Mosel, Phys. Rep. **512**, 1 (2012).
[10] J. Carlson, S. Gandolfi, F. Pederiva, S. C. Pieper, R. Schiavilla, K. E. Schmidt, and R. B. Wiringa, Rev. Mod. Phys. **87**, 1067 (2015).
[11] A. Lovato, S. Gandolfi, J. Carlson, S. C. Pieper, and R. Schiavilla, Phys. Rev. Lett. **117**, 082501 (2016).
[12] A. Lovato, S. Gandolfi, J. Carlson, E. Lusk, S. C. Pieper, and R. Schiavilla, Phys. Rev. C **97**, 022502 (2018).
[13] N. Rocco, C. Barbieri, O. Benhar, A. De Pace, and A. Lovato, Phys. Rev. C **99**, 025502 (2019).
[14] S. Pastore, J. Carlson, S. Gandolfi, R. Schiavilla, and R. B. Wiringa,arXiv:1909.06400.
[15] R. P. Feynman, Int. J. Theor. Phys. **21**, 467 (1982).

[16] S. Lloyd, Science **273**, 1073 (1996).
[17] A. Roggero and J. Carlson, Phys. Rev. C **100**, 034610 (2019).
[18] R. Somma, G. Ortiz, J. E. Gubernatis, E. Knill, and R. Laflamme, Phys. Rev. A **65**, 042323 (2002).
[19] D. Wecker, M. B. Hastings, N. Wiebe, B. K. Clark, C. Nayak, and M. Troyer, Phys. Rev. A **92**, 062318 (2015).
[20] P. F. Bedaque and U. van Kolck, Annu. Rev. Nucl. Part. Sci. **52**, 339 (2002).
[21] H. W. Hammer, S. König, and U. van Kolck, arXiv: 1906.12122.
[22] P. F. Bedaque, H.-W. Hammer, and U. van Kolck, Phys. Rev. Lett. **82**, 463 (1999).
[23] P. Bedaque, H.-W. Hammer, and U. van Kolck, Nucl. Phys. **A646**, 444 (1999).
[24] L. Contessi, A. Lovato, F. Pederiva, A. Roggero, J. Kirscher, and U. van Kolck, Phys. Lett. B **772**, 839 (2017).
[25] W. G. Dawkins, J. Carlson, U. van Kolck, and A. Gezerlis, arXiv:1908.04288.
[26] D. Lee, Prog. Part. Nucl. Phys. **63**, 117 (2009).
[27] B.-N. Lu, N. Li, S. Elhatisari, D. Lee, E. Epelbaum, and U.-G. Meißner, Phys. Lett. B **797**, 134863 (2019).
[28] M. Piarulli and I. Tews, Front. Phys. **7**, 245 (2020).
[29] A. Rokash, E. Epelbaum, H. Krebs, D. Lee, and U.-G. Meißner, J. Phys. G **41**, 015105 (2014).
[30] P. Jordan and E. Wigner, Z. Phys. **47**, 631 (1928).
[31] J. D. Whitfield, J. Biamonte, and A. Aspuru-Guzik, Mol. Phys. **109**, 735 (2011).
[32] J. Welch, D. Greenbaum, S. Mostame, and A. Aspuru-Guzik, New J. Phys. **16**, 033040 (2014).
[33] I. D. Kivlichan, C. Gidney, D. W. Berry, N. Wiebe, J. McClean, W. Sun, Z. Jiang, N. Rubin, A. Fowler, A. Aspuru-Guzik, H. Neven, and R. Babbush, arXiv: 1902.10673.
[34] G. H. Low and I. L. Chuang, Quantum **3**, 163 (2019).
[35] M. B. Hastings, D. Wecker, B. Bauer, and M. Troyer, Quantum Inf. Comput. **15**, 1 (2015).
[36] A. M. Childs and N. Wiebe, Quantum Inf. Comput. **12**, 901 (2012).
[37] D. W. Berry, A. M. Childs, R. Cleve, R. Kothari, and R. D. Somma, Phys. Rev. Lett. **114**, 090502 (2015).
[38] A. M. Childs, D. Maslov, Y. Nam, N. J. Ross, and Y. Su, Proc. Natl. Acad. Sci. U.S.A. **115**, 9456 (2018).
[39] H. F. Trotter, Proc. Am. Math. Soc. **10**, 545 (1959).
[40] M. Suzuki, J. Math. Phys. (N.Y.) **32**, 400 (1991).
[41] D. W. Berry, G. Ahokas, R. Cleve, and B. C. Sanders, Commun. Math. Phys. **270**, 359 (2007).
[42] F. Verstraete, J. I. Cirac, and J. I. Latorre, Phys. Rev. A **79**, 032316 (2009).
[43] I. D. Kivlichan, J. McClean, N. Wiebe, C. Gidney, A. Aspuru-Guzik, G. K.-L. Chan, and R. Babbush, Phys. Rev. Lett. **120**, 110501 (2018).
[44] S. A. Kutin, arXiv:quant-ph/0609001.
[45] G. H. Low and I. L. Chuang, Phys. Rev. Lett. **118**, 010501 (2017).
[46] D. Poulin, A. Kitaev, D. S. Steiger, M. B. Hastings, and M. Troyer, Phys. Rev. Lett. **121**, 010501 (2018).
[47] R. Babbush, C. Gidney, D. W. Berry, N. Wiebe, J. McClean, A. Paler, A. Fowler, and H. Neven, Phys. Rev. X **8**, 041015 (2018).
[48] E. Campbell, Phys. Rev. Lett. **123**, 070503 (2019).
[49] A. Peruzzo, J. McClean, P. Shadbolt, M.-H. Yung, X.-Q. Zhou, P. J. Love, A. Aspuru-Guzik, and J. L. O'Brien, Nat. Commun. **5**, 4213 (2014).
[50] 20qubit backed: IBM Q team, IBM Poughkeepsie backend specification v1.2.0 (2019), retrieved from https://quantum-computing.ibm.com.
[51] H. Abraham *et al.*, Qiskit: An open-source framework for quantum computing https://doi.org/10.5281/zenodo.2562111 (2019).
[52] Y. Li and S. C. Benjamin, Phys. Rev. X **7**, 021050 (2017).
[53] E. F. Dumitrescu, A. J. McCaskey, G. Hagen, G. R. Jansen, T. D. Morris, T. Papenbrock, R. C. Pooser, D. J. Dean, and P. Lougovski, Phys. Rev. Lett. **120**, 210501 (2018).
[54] S. Endo, S. C. Benjamin, and Y. Li, Phys. Rev. X **8**, 031027 (2018).
[55] J. J. Wallman and J. Emerson, Phys. Rev. A **94**, 052325 (2016).
[56] A. Roggero and A. Baroni, Phys. Rev. A **101**, 022328 (2020).
[57] A. Kandala, K. Temme, A. D. Córcoles, A. Mezzacapo, J. M. Chow, and J. M. Gambetta, Nature (London) **567**, 491 (2019).
[58] K. Temme, S. Bravyi, and J. M. Gambetta, Phys. Rev. Lett. **119**, 180509 (2017).
[59] S. Endo, Q. Zhao, Y. Li, S. Benjamin, and X. Yuan, Phys. Rev. A **99**, 012334 (2019).
[60] W. K. Wootters, Phys. Rev. Lett. **80**, 2245 (1998).
[61] S. Hill and W. K. Wootters, Phys. Rev. Lett. **78**, 5022 (1997).
[62] A. Barenco, C. H. Bennett, R. Cleve, D. P. DiVincenzo, N. Margolus, P. Shor, T. Sleator, J. A. Smolin, and H. Weinfurter, Phys. Rev. A **52**, 3457 (1995).
[63] D. Wecker, B. Bauer, B. K. Clark, M. B. Hastings, and M. Troyer, Phys. Rev. A **90**, 022305 (2014).
[64] S. S. Bullock and I. L. Markov, Quantum Inf. Comput. **4**, 27 (2004).
[65] N. Schuch (2002).
[66] F. Vatan and C. Williams, Phys. Rev. A **69**, 032315 (2004).
[67] V. Bergholm, J. J. Vartiainen, M. Möttönen, and M. M. Salomaa, Phys. Rev. A **71**, 052330 (2005).
[68] D. Maslov, Phys. Rev. A **93**, 022311 (2016).